Article

Foundation Alternative for Bridges in Liquefiable Soils

Nohemí Olivera and Juan Manuel Mayoral *

Posted Date: 7 May 2026

doi: 10.20944/preprints202605.0415.v1

Keywords: liquefaction; bridges; seismic soil-structure interaction; lateral spreading; foundations

 doi:10.20944/preprints202605.0415.v1

Article

Foundation Alternative for Bridges in Liquefiable Soils

Nohemí Olivera and Juan Manuel Mayoral *

Geotechnical Department, Institute of Engineering, National University of Mexico, Mexico City 04510, Mexico

* Correspondence: jmayoralv@iingen.unam.mx

Abstract

Ground failure during major seismic events associated with soil liquefaction can lead to major structural damage in both the columns and the bridge upper deck, due to large seismic-induced displacements in the support foundation. Liquefaction-driven ground motion incoherence during the dynamic event, and permanent soil deformations are key variables in the observed damage. This paper summarizes a numerical study of an alternative bridge foundation design proposed to reduce support displacements and bearing capacity failure during and after an earthquake, as well as relative settlement associated with partial loss of bearing capacity when the bridge column is founded on a potential liquefiable layer. Three-dimensional numerical models were developed using FLAC^{3D}. The seismic environment was characterized by a uniform hazard spectrum, UHS, for intraplate and interplate earthquakes, as presented in the current construction Mexico City regulations. Initially, a one-dimensional analysis was performed using SHAKE to evaluate liquefaction susceptibility. Results show that the structured cell foundation reduces excess pore pressure generation by up to 42% compared to shallow foundations and 25% compared to pile systems. This improvement is associated with (i) restriction of cyclic shear strain, (ii) modification of deformation patterns, (iii) partial hydraulic isolation of the confined soil, and (iv) preservation of effective stresses during shaking. Additionally, the system reduces shear strain localization and decreases acceleration transmitted to the superstructure by up to 25%. The findings demonstrate that structured confinement systems can significantly alter the mechanisms governing liquefaction, offering a promising alternative for bridge foundations in seismic regions.

Keywords: liquefaction; bridges; seismic soil-structure interaction; lateral spreading; foundations

1. Introduction

Soil liquefaction is defined as the loss of strength resulting from the reduction in effective stress caused by excess pore pressure generated during cyclic loading of uncompacted non-plastic fine-grained soil, such as silty sands and sandy silts. Although it occurs mostly in loose, saturated sands, it has also been observed in gravel and non-plastic silts. This gradual loss of strength reduces bearing capacity, which, in turn, may preclude adequate structural performance due to permanent ground movements and lateral spreading. Poor performance of bridge foundations under seismic loading was observed during the Niigata [1] and Anchorage earthquakes [2]. Similarly, during the 1989 Loma Prieta, 1994 Northridge [3], and 1995 Kobe earthquakes [4].

In Mexico, during the 2010 Mexicali earthquake, a section of the San Felipito bridge collapsed [5] due to lateral soil displacement caused by ground liquefaction. In bridge structures, pile foundations have been used extensively in both liquefiable and non-liquefiable soils. In liquefiable soils, the progressive buildup of pore water pressure can lead to a loss of strength and stiffness, resulting in large bending moments and shear forces in the pile [6,7].

The behavior of piles in liquefiable soils has been studied by various researchers over the past few decades [8–11]. Karamitros et al. [12] analyze the estimation of post-shaking bearing capacity of shallow foundations located on liquefiable soils through numerical finite-difference models.

 doi:10.20944/preprints202605.0415.v1

Likewise, other researchers have examined the impact of strength loss using results from physical model tests and numerical simulations [13]. The damage caused by liquefaction can be reduced with soil improvement techniques, increasing its strength and reducing compressibility. Conventional techniques, including chemical cement and grout, compaction, and soil reinforcement, have been used for many decades [14–18]. Various methods have recently been developed that include novel materials such as nanomaterials, synthetic fibers, recycled materials, biopolymers, and biomaterials [19,20].

While these approaches have proven effective, they may involve high construction costs or limited efficiency under complex soil–structure interaction conditions. In this context, alternative foundation systems capable of reducing pore pressure generation and controlling soil deformation demand further investigation.

In this work, a structured cell foundation alternative is proposed for bridge supports founded in potentially liquefiable soil deposits, and its behavior is evaluated using three-dimensional finite-difference models with FLAC^{3D} software [21]. To represent the behavior of the liquefiable stratum, a constitutive model that accounts for the generation of excess pore pressures is used. The specific contributions of this study are threefold. First, the mechanisms of liquefaction mitigation associated with structured cell foundations are quantified in terms of excess pore pressure generation, effective stress reduction, and shear strain accumulation. Second, a comparative performance assessment of three foundation alternatives, spread footing, pile group, and structured cell, is carried out under identical seismic loading conditions, allowing a consistent evaluation of their relative effectiveness. Third, the transmission of seismic demand to the bridge superstructure is evaluated through response indicators such as peak accelerations and Housner intensity.

The results provide new insight into how structural confinement modifies the fundamental response of liquefiable soils, contributing to the development of more efficient foundation design strategies in seismic regions.

2. Case Study

As depicted in Figure 1, the studied bridge is considered to be located in the northwestern area of the State of Mexico, in the Trans-Mexican Volcanic Belt in the center of Mexico, belonging to the physiographic province of the Neovolcanic Axis, which is characterized by an andesitic porphyry type igneous rock formation and alluvial deposits. The upper deck of the bridge consists of Nebraska NU/240 beams, resting on four supports and two abutments, as shown in Figure 2. The bridge consists of 6 supports, is 230 m long, with a total width of 22.06 m, and a roadway width of 21 m. The deck sections 1 to 5 are supported on reinforced concrete trestles and hollow columns with spans of 46 m. The supports are monolithically joined with foundation shoes. The geometry of the foundation footings is 7.00 m wide, 24.00 m long, and 2.00 m thick. Table 1 presents the characteristics of the main components of the structure.

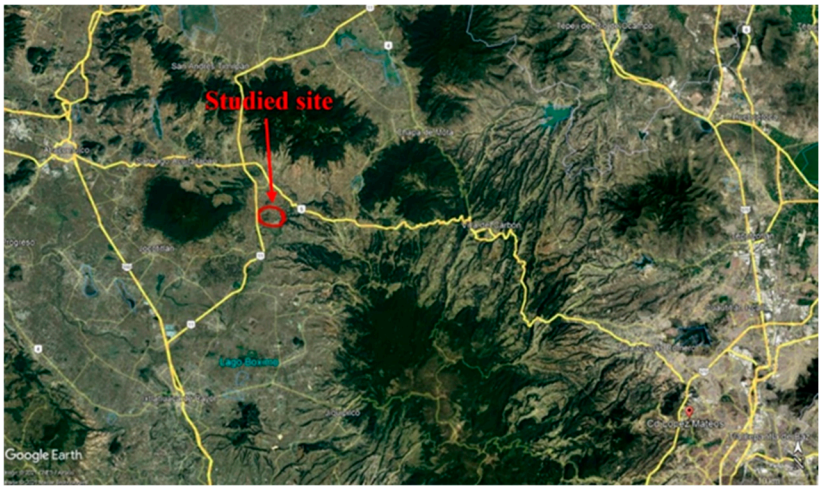

 doi:10.20944/preprints202605.0415.v1

Figure 1. Case study location, nearby faults, and seismological stations.

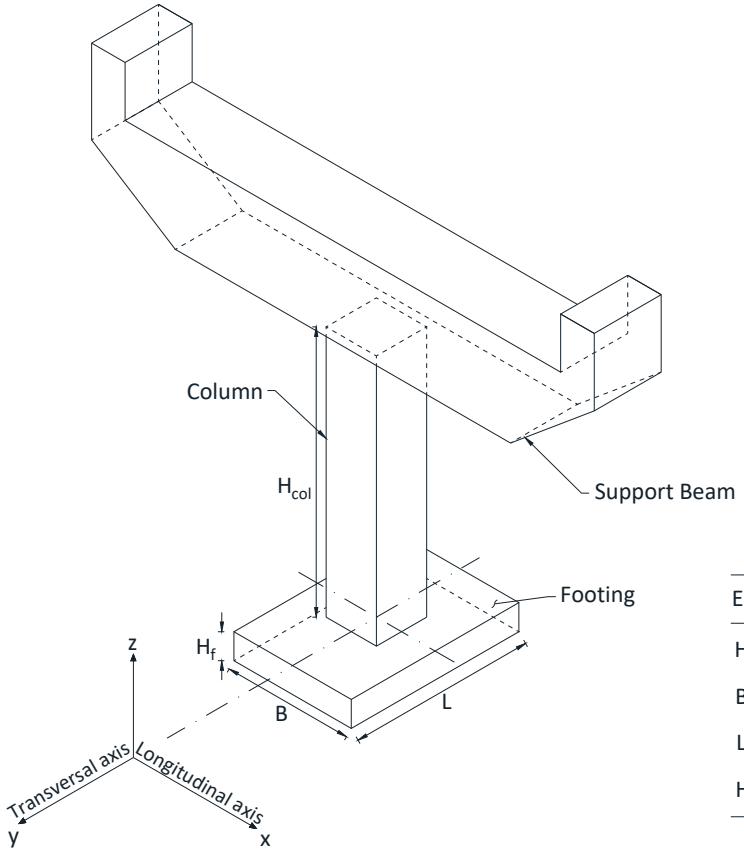

Element	Dimension, m
H_f, footing thickness	1.5
B, footing width	7.0
L, footing length	10.0
H_{col}, column height	12.0

Figure 2. Schematic representation of bridge supports.

Table 1. Structural characteristics of the support structure.

Element	**f¨c** **kPa**	**E** **MPa**	
Footing	29420	25629	0.20
Column	50500	30000	0.20
Support Beam	50500	30000	0.20

2.1. Subsoil Conditions Characterization

To characterize the geotechnical subsoil conditions under supports A-1 to A-6, 21 standard penetration tests with selective undisturbed sample recovery were conducted. Based on this field investigation, it was established that the soil profile deposit is mainly comprised of sands, clays, and andesitic rock. Figure 3 presents the geotechnical soil profile obtained from exploration along the bridge. The control points indicated in the profile (i.e., A-1, A-2, A-3, A-4, A-5, A-6) correspond to the bridge support locations. The geotechnical properties obtained are presented in Table 2. As can be seen, the geotechnical unit No. 16 corresponds to loose sand, just below the support A-4.

 doi:10.20944/preprints202605.0415.v1

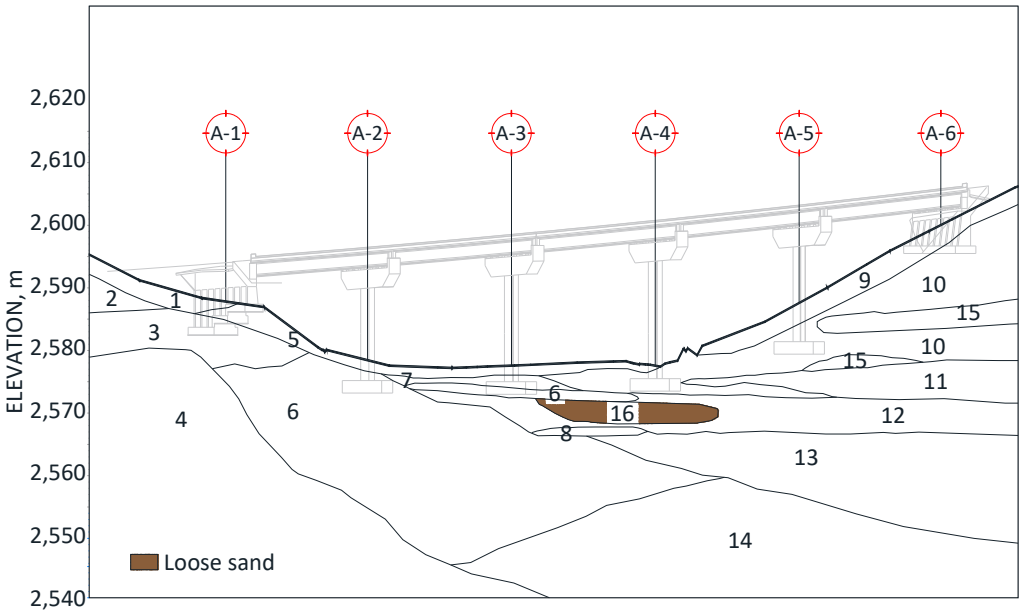

Figure 3. Geotechnical soil profile.

Table 2. Soil properties used in the analysis.

Geotechnical units	γ* (kN/m³)	c (kPa)	f (°)	Description
UG-1	17.0	30	27	Low plasticity clay
UG-2	18.0	30	30	Low and high plasticity clays of hard consistency
UG-3	18.0	30	30	Low and high plasticity clays
UG-4	20.0	112	24	Agglomerate, RQD (0-100%)
UG-5	17.0	24	25	Low and high plasticity clays of soft to medium consistency
UG-6	18.8	38	36	Sequence of clayed sands with gravels
UG-7	20.0	355	31	Basalt, RQD (0-46%)
UG-8	23.0	172	36	Rhyolite, RQD (24%)
UG-9	16.7	116	34	Silty and clayed sand of medium to very dense compactness
UG-10	19.5	685	32	Silty sand with gravel and clay
UG-11	19.6	152	33	Rhyolite, RQD (0%)
UG-12	20.9	73.6	36	Agglomerate, RQD (0-46%)
UG-13	19.0	355	31	Gravel
UG-14	21.5	72.8	17	Agglomerate, RQD (25-57%)
UG-15	21.0	72.1	17	Agglomerate, RQD (20-71%)
UG-16	18.0	9.3	25	Loose sand

*γ, is the unit weight, c, cohesion, and f the friction angle.

Shear wave velocity profiles were determined with the empirical expressions presented in Table 3. Further, these expressions are a function of the uncorrected SPT blow counts value NSPT and were calibrated with three cross holes, CH-1 to CH-3, carried out in similar materials. Shear wave velocity profiles determined with the cross-hole technique were compared for completeness with those obtained from the empirical expressions presented in Table 3. As shown in Figure 4, there is good agreement between the measured and estimated Vs profiles. Figure 5 presents the shear wave velocity and the idealized geotechnical soil profile for support A-4.

 doi:10.20944/preprints202605.0415.v1

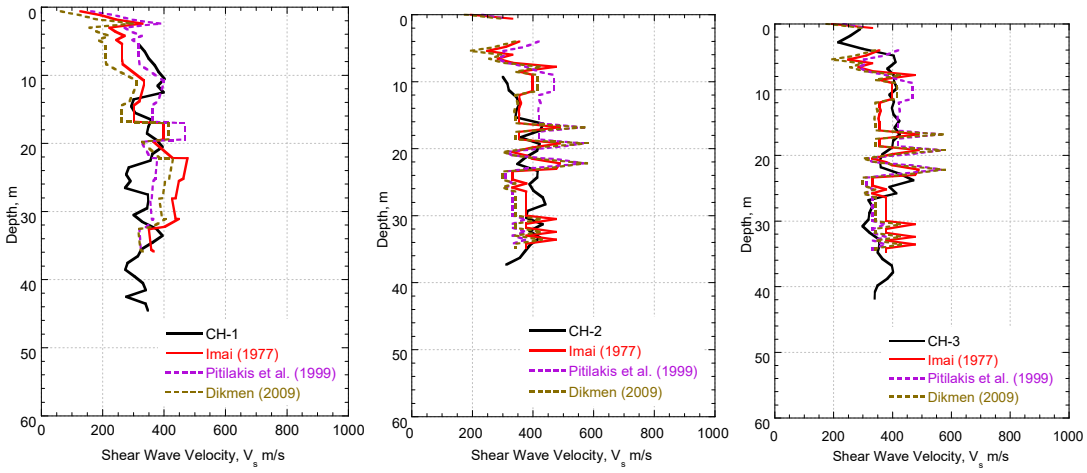

Figure 4. Comparison between the shear wave velocity measured and estimated, and SPT N values for each CH considered.

Table 3. Empirical correlations used to estimate the shear wave velocity distributions at the site.

Author	Correlations	
	For sands	For clays
Imai [22]	$V_s = 80.6\ N^{0.331}$	$V_s = 102\ N^{0.292}$
Pitilakis et al. [23]	$V_s = 145\ N_{60}{}^{0.178}$	$V_s = 132\ N_{60}{}^{0.271}$
Dikmen [24]	$V_s = 73\ N^{0.33}$	$V_s = 44\ N^{0.48}$

Where N is the uncorrected SPT blow counts value.

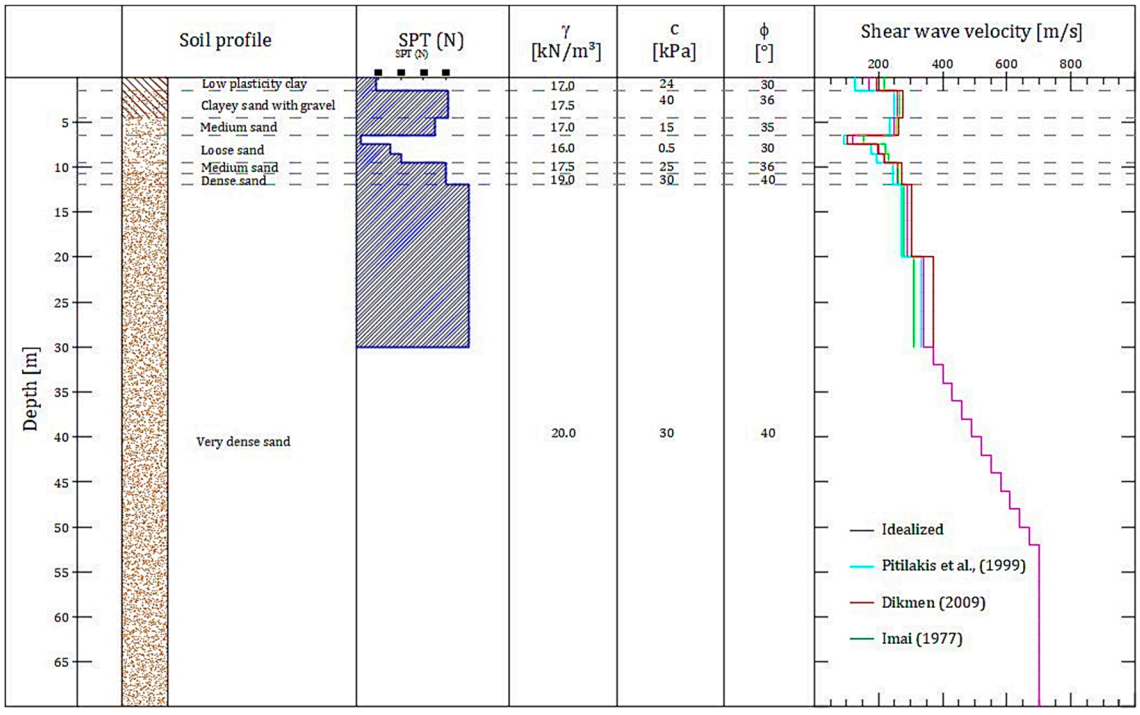

Figure 5. Shear wave velocity and geotechnical soil profile idealized for the support A-4.

2.2. Dynamic Properties

Due to the lack of experimental and laboratory information from the study area, to define the dynamic properties of the materials it was considered to use a loose sand with known properties employed by various researchers [25,26], while for cohesive materials it was considered appropriate

 doi:10.20944/preprints202605.0415.v1

to use the Vucetic and Dobry [27], as a function of plasticity index, PI considering the information gathered from index properties criterion and due to the good approximation of the behavior with experimental tests reported in the literature [28,29]. Soil nonlinearity was also considered using a hysteretic damping approach (Figure 6).

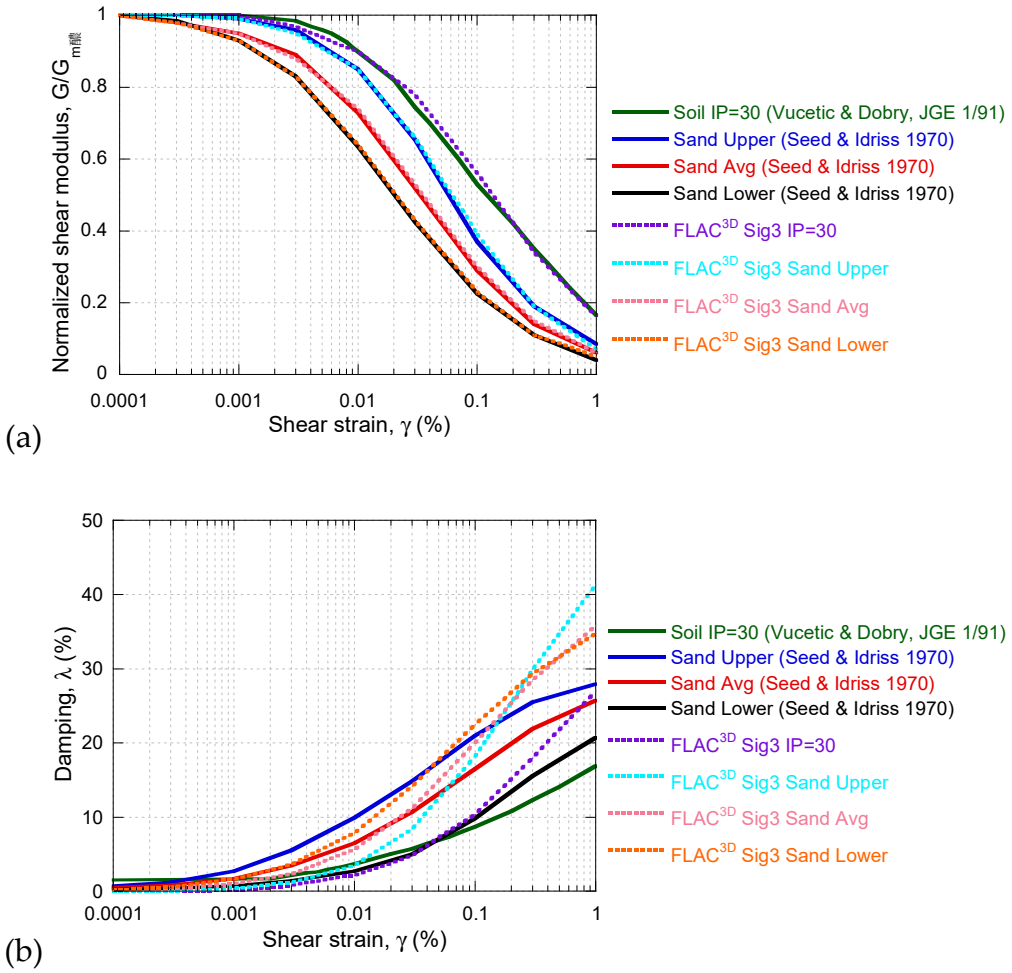

Figure 6. Curves of (a) normalized modulus degradation, G / G_{max}, and (b) damping, λ.

2.3. Seismic Environment

Initially, the seismic soil-structure interaction was analyzed considering the set of six ground motions compiled in Table 4, with varying duration and frequency characteristics. These strong ground motions were recorded in firm soil or rock. Mexico City is exposed to seismic hazards from interplate earthquakes along the Mexican subduction zone (i.e., interplate events) and intraslab earthquakes generated in the subducted Cocos plate (i.e., intraplate events). The area is also subject to relatively infrequent local and regional crustal earthquakes in the Trans-Mexican volcanic belt [30]. The largest earthquakes in Mexico City along the Pacific coast are caused by the subduction of the oceanic Cocos and Rivera plates beneath the North American plate at depths of approximately 40-180 km [31]. Large-magnitude earthquakes also occur on the continent, with depths ranging from 30 to 100 km. In this case, earthquakes present a normal faulting mechanism that reflects the breaking of the subduced oceanic lithosphere [32]. The seismic environment was established using uniform hazard spectra for a return period of 250 years, as recommended in the Mexico City building code [33], considering interplate and intraplate events, based on seismogenic activity along the faults that control risk in Mexico City. The Mexican code recommends a return period of 250 years for the seismic design of structures, which is related to, in the case of interplate events, an event with a magnitude of 7.8 at a focal length of 265 km; and for intraplate events, the dominant earthquake has

 doi:10.20944/preprints202605.0415.v1

a magnitude of 7.5 and a focal length of 110 km [34]. These are the most likely scenarios based on current knowledge of the seismic source characteristics, including the rupture area and the distance from the energy release zone to the city. According to the ASCE/SEI Standard 7–10, when the required number of recorded ground motions is not available, appropriate simulated ground motions are permitted to be used to make up the total number required [35].

Table 4. Earthquakes considered in the analyses.

Seismogenic zone	Earthquake name	Year	Mw, Moment magnitude	PGA, Peak ground acceleration (g)	TD (s)	Frequency content (Hz)	Arias intensity (cm/s)
Intraplate	Montenegro (former Yugoslavia), MONTE	1979	6.9	0.251	12.1	0.18 to 3.0	46.8
	Umbria Marche (Gubbio-Piana, Italy), UMBRIA	1998	4.8	0.223	2.3	0.2 to 4.6	18.2
	Puebla-Mexico City (CU, Mexico), CU17	2017	7.1	0.059	29.6	0.23 to 3.5	12.7
Interplate	Michoacan (CU, Mexico), CU85	1985	8.1	0.033	49.7	0.38 to 1.36	15.5
	Maule (Concepcion San Pedro, Chile), CHILE	2010	8.8	0.638	71.2	0.46 to 1.34	1418.5
	Honshu (Haga, Japan), JAPAN	2011	9	0.939	68.3	0.31 to 1.26	136.4

Note: TD is the significant duration of ground motion defined as the difference between T-95 and T-5, which are respectively the times where 95% and 5% of Arias intensity is reached.

To develop an acceleration time history in which the response spectrum reasonably matches the design response spectrum for the return period of analysis (i.e., T = 250 years), the selected time history, usually called seed ground motion, was modified using the method proposed by Lilhanand and Tseng [36] as modified by Abrahamson [37]. This approach modifies the acceleration history to make it compatible with a user-specified target spectrum. The time history can be modified using various models. In doing so, the long-term non-stationary phasing of the original time history is preserved. The 5% damp response spectra calculated for the modified time histories are compared with the target UHS in Figures 7 and 8. The response spectrum calculated from the modified time histories reasonably matches the target spectrum.

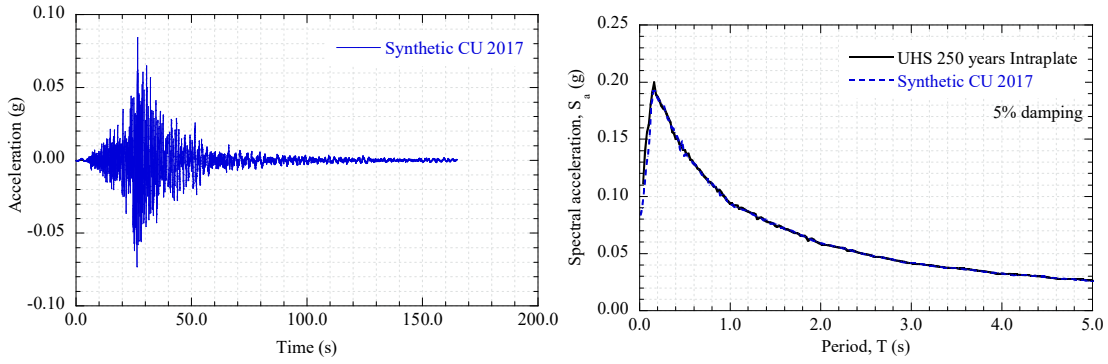

(**a**)

 doi:10.20944/preprints202605.0415.v1

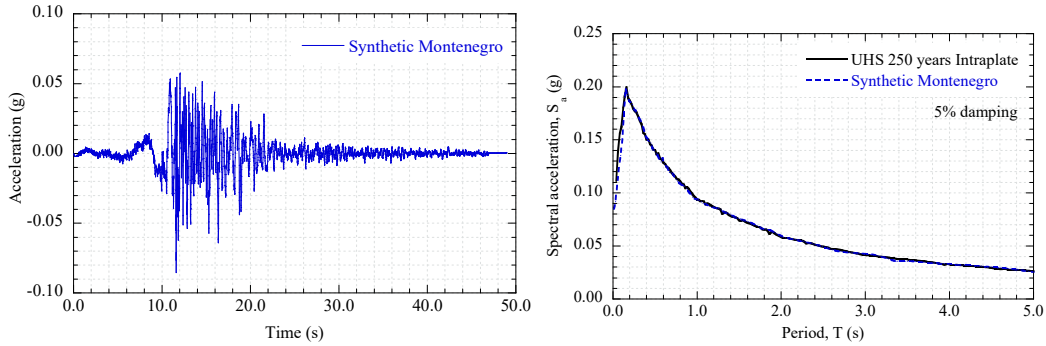

(**b**)

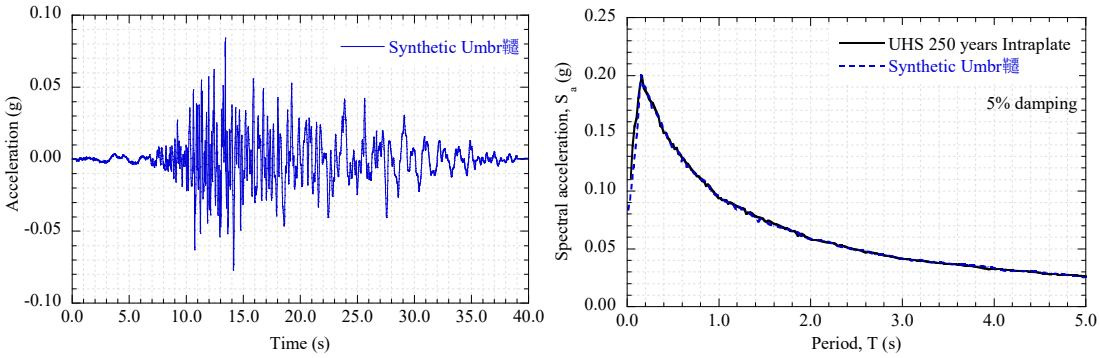

(**c**)

Figure 7. Synthetic time histories, uniform hazard spectra, and adjusted ground motion response spectra for intraplate events, (a) CU 2017, (b) Montenegro, and (c) Umbria.

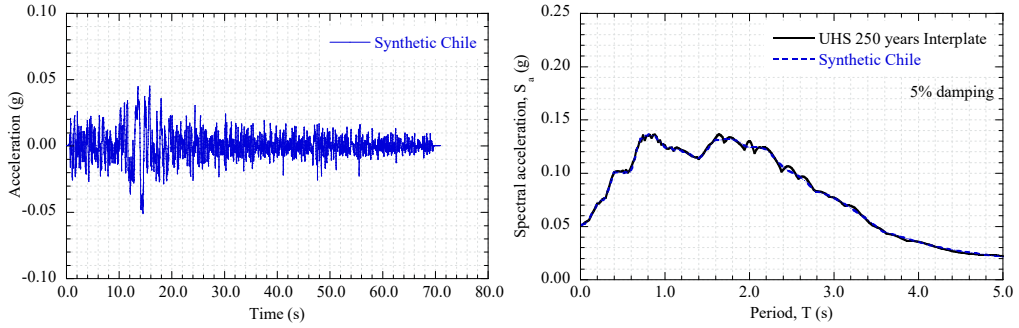

(a)

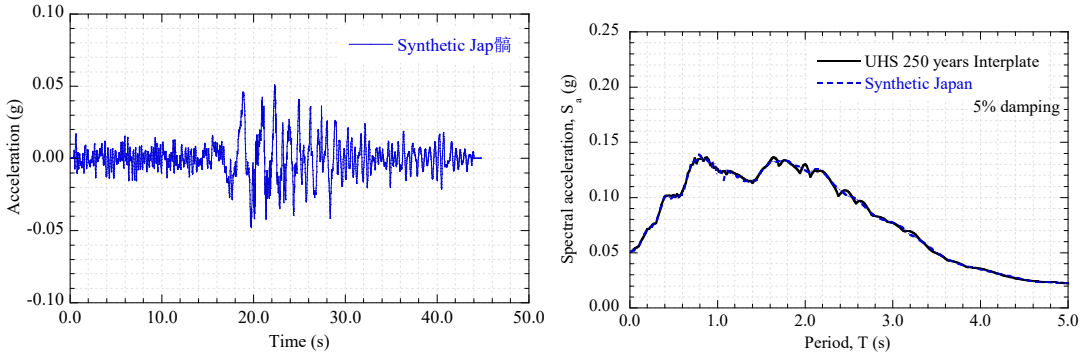

(b)

 doi:10.20944/preprints202605.0415.v1

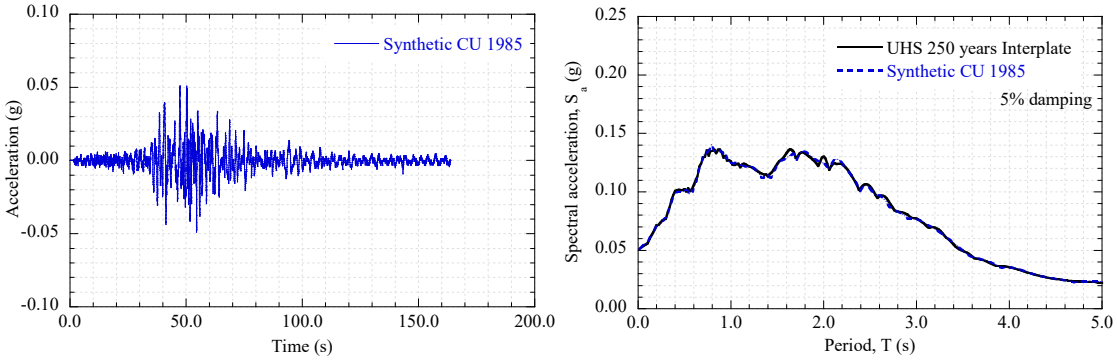

(c)

Figure 8. Synthetic time histories, uniform hazard spectra, and adjusted ground motion response spectra for interplate events, (a) Chile, (b) Japan, and (c) CU 1985.

3. Assessment of Liquefaction Potential

To determine the liquefaction potential, the widely used CPT and SPT-based simplified procedure, based on the empirical method originally proposed by Seed & Idriss [38] and Seed et al. [39], as summarized in the NCEER by Youd et al. [40], and more recently by Idriss & Boulanger [41], and Boulanger & Idriss [42]. In the simplified procedure, it is required to estimate the cyclic stress ratio (CSR), which represents the seismic demand on a soil layer due to the design earthquake shaking, and the cyclic resistance ratio (CRR), which represents the soil's capacity to withstand liquefaction. Based on the geotechnical characterization shown in Figure 5, models were developed for one-dimensional site response analysis using the SHAKE [43] computer code, which performs an equivalent linear analysis in the frequency domain. Figure 9 shows the results of the Standard Penetration Test SPT, N_{60}, CSR, and safety factors obtained for the soil profile of support A-4. As shown, the localized granular soil stratum at 6.50-9.50 m is potentially liquefiable; that is, the cyclic stress ratio induced by the earthquake exceeds the cyclic resistance ratio.

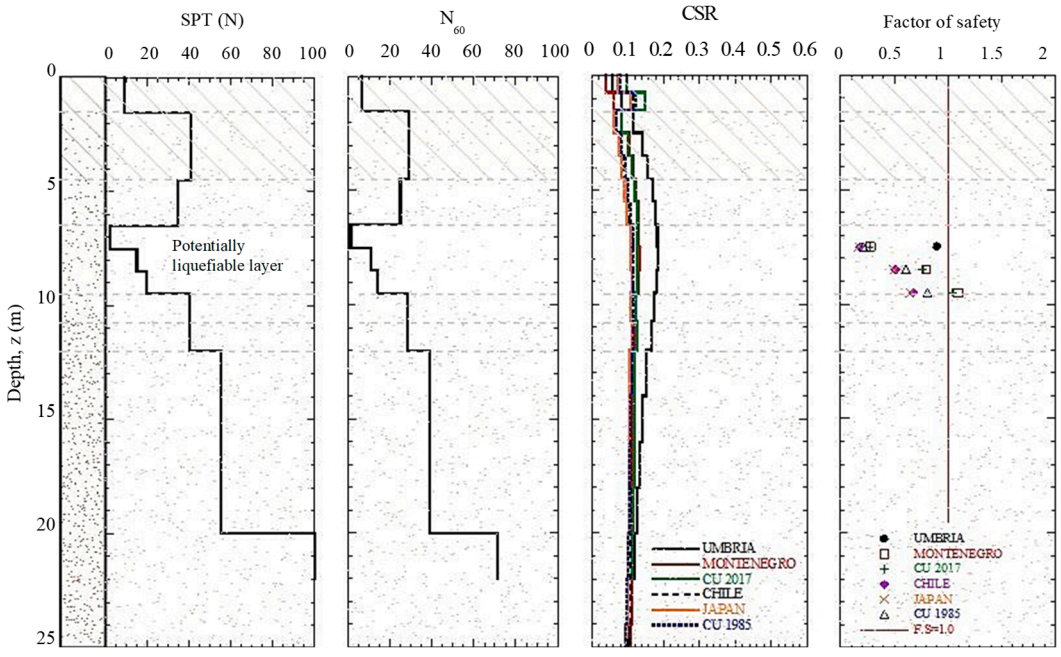

Figure 9. Liquefaction potential for support A-4.

 doi:10.20944/preprints202605.0415.v1

4. Numerical Model

A three-dimensional finite-difference model was developed in FLAC^{3D} [21], as depicted in Figure 10. An elastoplastic Mohr-Coulomb model was used to simulate the soil's stress relationship. The model has 62319 elements and 67157 nodes. A fully non-linear site response analysis was carried out using FLAC^{3D} to further investigate soil nonlinearity. The finite differences model has a total depth of 70.0 m. Free-field boundaries were implemented along the model's edges, and a flexible base was used at the bottom. From a seismic standpoint, the thicknesses of the elements were selected based on the geometry and size of the soil layers. However, as is well known, numerical distortion of the propagating wave can occur in a dynamic analysis as a function of modeling conditions [21]. Therefore, both the frequency content of the input wave and the system's wave-speed characteristics will affect the numerical accuracy of wave transmission. In the case studied herein, the recommendation by Kuhlemeyer and Lysmer [44] for the spatial element size, ΔL, is to accurately represent wave transmission in the numerical models employed. Therefore, ΔL was kept smaller than one-fifth of the wavelength associated with the highest frequency component of the input wave that contains appreciable energy, fmax (i.e., $\Delta L \leq \lambda/5$). The shortest wavelength L is given by L = Vs/fmax. For the problem at hand, the smallest average shear wave velocity, Vs, of the studied site in the less stiff upper soils (i.e., upper 10 m of the sand) was about 120 m/s, as can be seen in Figure 5, and the highest significance of the excitation where the energy is concentrated is around 1-5 Hz. Hence, a ΔL of 2 m was deemed appropriate.

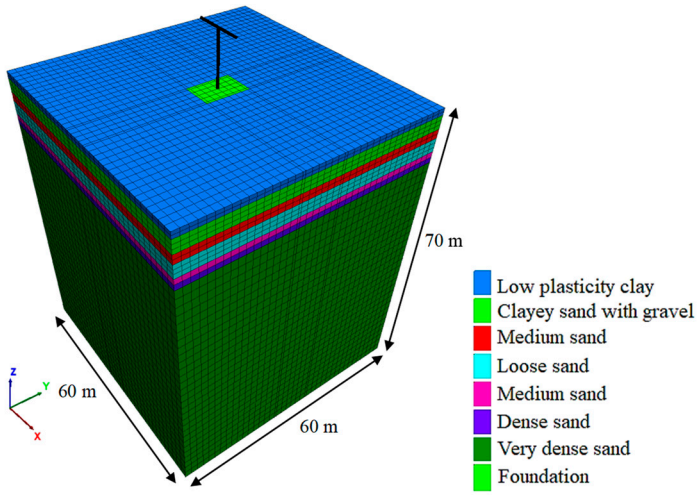

(**a**)

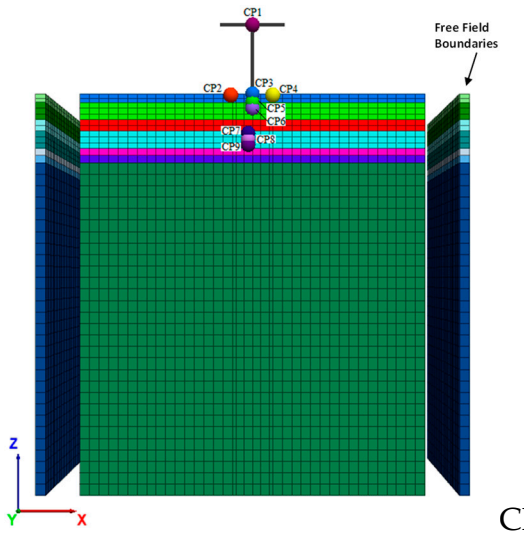

CP: Control point

 doi:10.20944/preprints202605.0415.v1

(b)

Figure 10. (a) Numerical model and (b) control points.

4.1. Constitutive Model for Non-Liquefiable Material

The practically oriented hysteretic model available in FLAC3D, denoted "sig3," was used to approximately account for both modulus stiffness degradation and damping variation during the seismic event. This model assumes an ideal soil in which stress depends only on deformation, not on the number of cycles. With these assumptions, the incremental constitutive relationship of the degradation curve can be described by $\tau n/\gamma = G/G_{max}$, where τn is the normalized shear stress, γ is the shear strain, and G/G_{max} is the normalized secant modulus.

The sig3 model is defined according to Eq. (1):

$$\frac{G}{G_{máx}} = \frac{a}{1 + exp\left(-\frac{L - x_0}{b}\right)} \quad (1)$$

where L is the logarithmic strain defined as $L = log10(\gamma)$, and the parameters a, b, and x_0, used by the sig3 model, were obtained by an iterative approach, in which the modulus degradation curves were fitted with the model equations. The corresponding damping is given directly by the hysteresis loop during cyclic loading. For the cases studied herein, the parameters "a", "b", and xo vary from 1.005 to 1.020, -0.47 to -0.56, and -0.89 to -1.7, respectively. Nonlinear soil behavior depends on the shaking level; at high levels, shear stiffness degrades and damping increases. The fact that FLAC3D generates higher damping at high strains than experimentally derived curves is due to the well-known limitation of hysteretic-type models, which cannot fully capture both shear stiffness degradation and damping curves developed under steady-state conditions. However, in a nonlinear analysis, it is attempted to characterize the transient ground response in each loading cycle as a function of the evolution of shear strains during ground shaking, rather than the steady state response established in the resonant column and cyclic triaxial test from which modulus degradation and damping curves, such as the Seed and Idriss model, were developed.

4.2. Constitutive Model for Liquefiable Material

To take into account a stress-strain law that includes shear-volume coupling effects for repeated load cycles, the constitutive model developed by Finn et al. [45] and Byrne [46] and calibrated by García et al. [47], Iraji and Osouli [48], and Chou et al. [49], was used. This model predicts expected volume changes and settlements due to liquefaction of saturated sands in dynamic analysis. For the random pattern of strain cycles, volumetric strains per half cycle are computed as:

$$\frac{(\Delta\epsilon_{vd})_{1/2cycle}}{\gamma} = C_1 \cdot exp\left(-C_2\left(\frac{\epsilon_{vd}}{\gamma}\right)\right) \quad (2)$$

Where ϵ_{vd} is the volumetric strain, γ is the strain amplitude of cyclic shear strain, and C_1 and C_2, are model input constants. C_1 controls the amount of volume change, and C_2 controls the shape of the accumulated volume changes with the number of cycles. Both C_1 and C_2 are related to the relative density of sand. Following Byrne (1991), the input parameters C_1 and C_2 are related to an intermediate parameter C_1^c, which depends on soil density conditions. In this study, C_1^c was estimated using an empirical correlation based on the normalized standard penetration resistance $(N_1)_{60}$ (Equation 3). The model input parameters were obtained using equations 4 and 5.

$$C_1^c = 8.7(N_1)_{60}^{-1.25} \quad (3)$$

$$C_1 = \frac{1}{2}C_1^c \quad (4)$$

 doi:10.20944/preprints202605.0415.v1

$$C_2 = \frac{0.4}{C_1^c} \quad (5)$$

The model captures key aspects of liquefaction behavior, including progressive pore-pressure buildup, effective stress reduction, and cyclic strain accumulation that leads to strength degradation. However, it should be noted that the Finn–Byrne formulation is a simplified approach and does not explicitly simulate pore-fluid migration or post-liquefaction reconsolidation. Table 5 presents the final parameters used in the numerical models

Table 5. Input parameters for the Finn-Byrne model of the loose sand layer.

Depth (m)		Shear modulus G (kPa)	Young modulus E (MPa)	c (kPa)	n (-)	ϕ (°)	$(N_1)_{60}$	C1	C2
6.50	7.50	23490	61.78	0.50	0.32	30	2	1.83895	0.10935
7.50	8.50	65240	171.61	0.50	0.32	30	15	0.14736	1.35723
8.50	9.50	78940	207.65	0.50	0.32	30	20	0.10285	1.94459

4.3. Free Field Response

Three-dimensional finite difference models of the free field were developed using FLAC^{3D} [21]. The ground motions compiled in Table 4, recorded at a rock outcrop, were used in the analyses. The ground motions were deconvolved to the base of each model using the software SHAKE [43]. The finite differences model of the free field has a depth of about 70 m and a 60 m by 60 m square section. The free-field boundaries implemented in FLAC^{3D} were used along the entire model. Figure 11 compares the horizontal computed response spectra obtained with SHAKE (Equivalent linear analysis) and FLAC^{3D} (Nonlinear analysis).

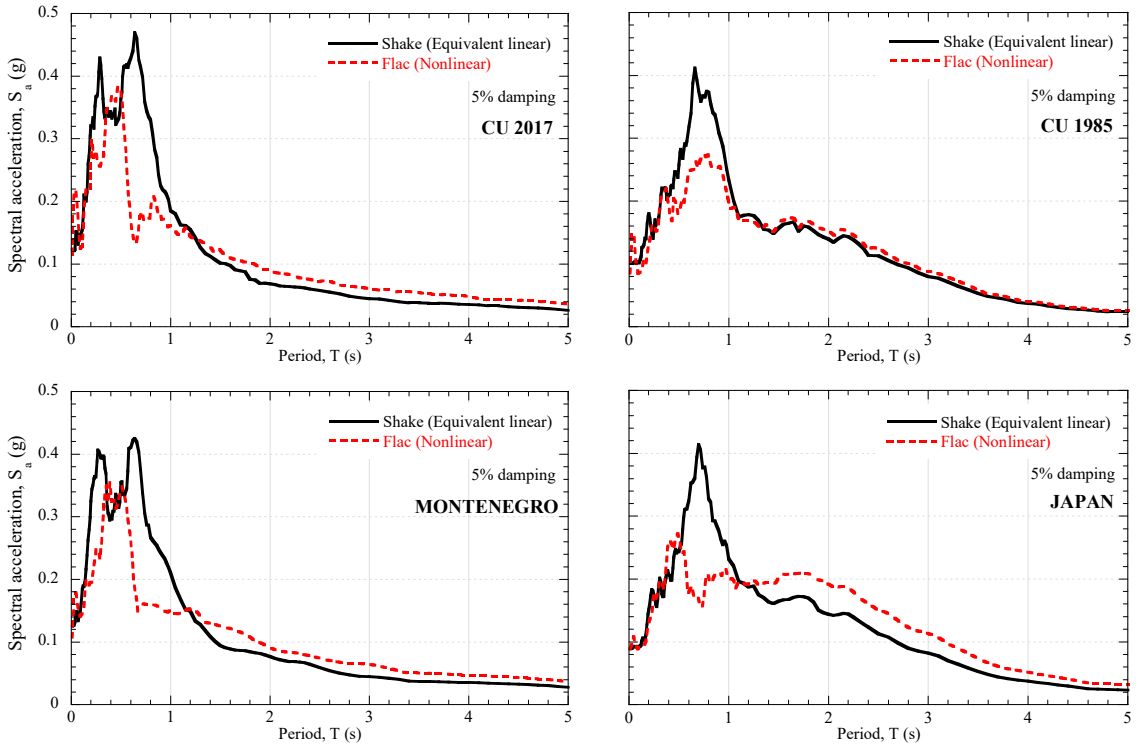

 doi:10.20944/preprints202605.0415.v1

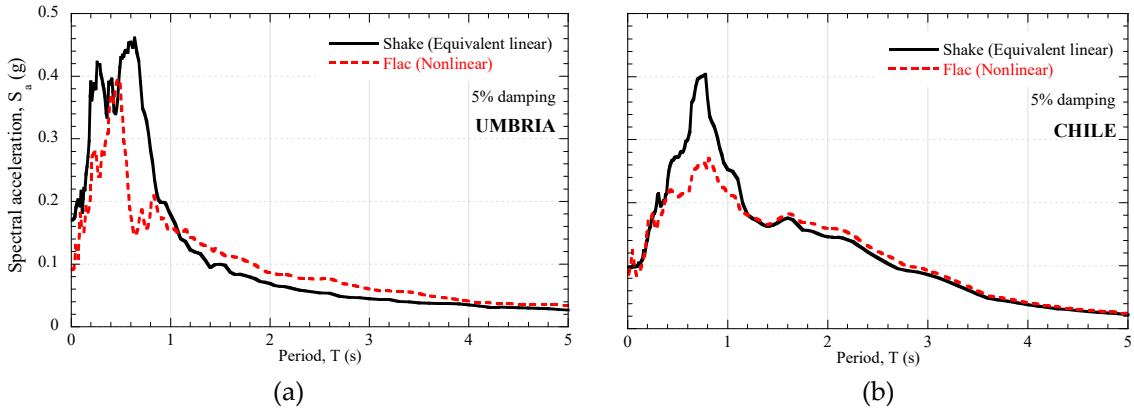

Figure 11. Horizontal computed response spectra in the free field obtained with SHAKE and FLAC^{3D} for (a) intraplate events and (b) interplate events.

4.4. Seismic Soil Structure Interaction

Figure 12 shows the three-dimensional finite-difference model used for the seismic soil-structure interaction analyses. The columns and frames were modeled with beam elements. Table 6 summarizes the corresponding material properties considered in the numerical model. Three alternatives for the foundation were considered: 1) Conventional foundation with footing, 2) structured cell, and 3) piles. A structured cell is comprised of a top concrete slab structurally connected to concrete external walls that enclose the natural soil [50] (Figure 13). To represent the elastoplastic behavior of the soil, the Mohr-Coulomb failure criterion was used, while for the liquefiable soil, the Finn and Byrne [45,46] model was implemented. The concrete strength at 28 days, f'c, was 25 MPa.

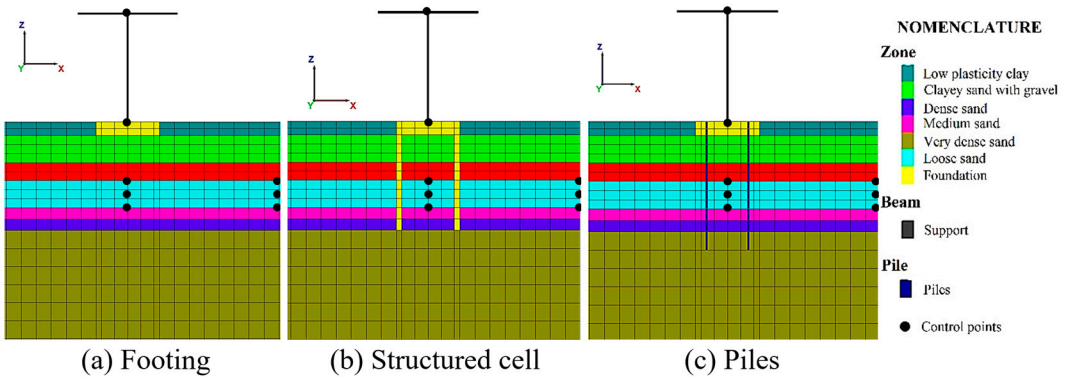

Figure 12. Three-dimensional finite difference for the case study, and the foundations used in the analysis: (a) Footing, (b) structured cell, and (c) piles.

Table 6. Properties of support substructure elements.

Element	f'c (kPa)	n (-)	E (MPa)
Footing	29420	0.20	25225
Concrete slab	29420	0.20	25225
Concrete perimeter wall	29420	0.20	25225
Piles	29420	0.20	25225

 doi:10.20944/preprints202605.0415.v1

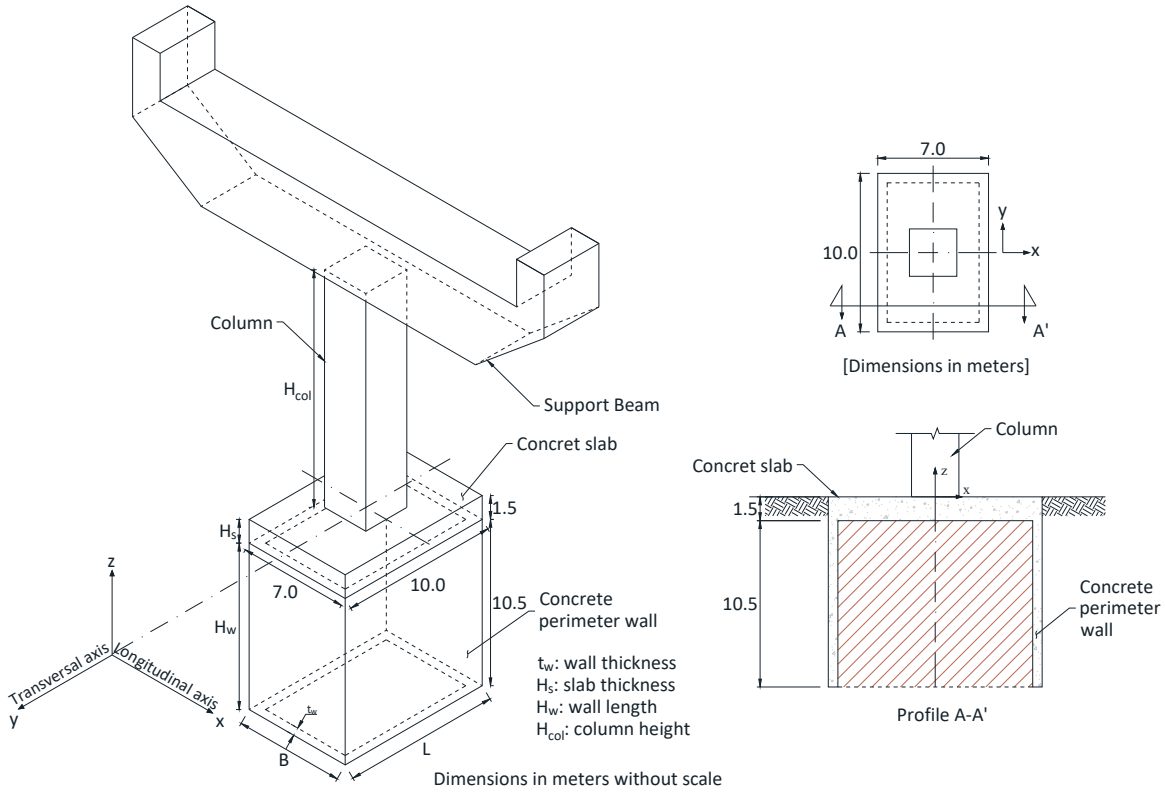

Figure 13. Schematic representation of the structured cell.

The bridge superstructure was idealized as a beam system with an equivalent density in the upper deck to simulate the mass distribution and account for the real superstructure's rocking effects [51] (Figure 14). This assumption was based on the fact that, for the cases studied herein, the support beam and the deck are structurally tied to the column. Thus, for the column and raft foundation, Young's modulus was set to 30,000 MPa and Poisson's ratio to 0.2.

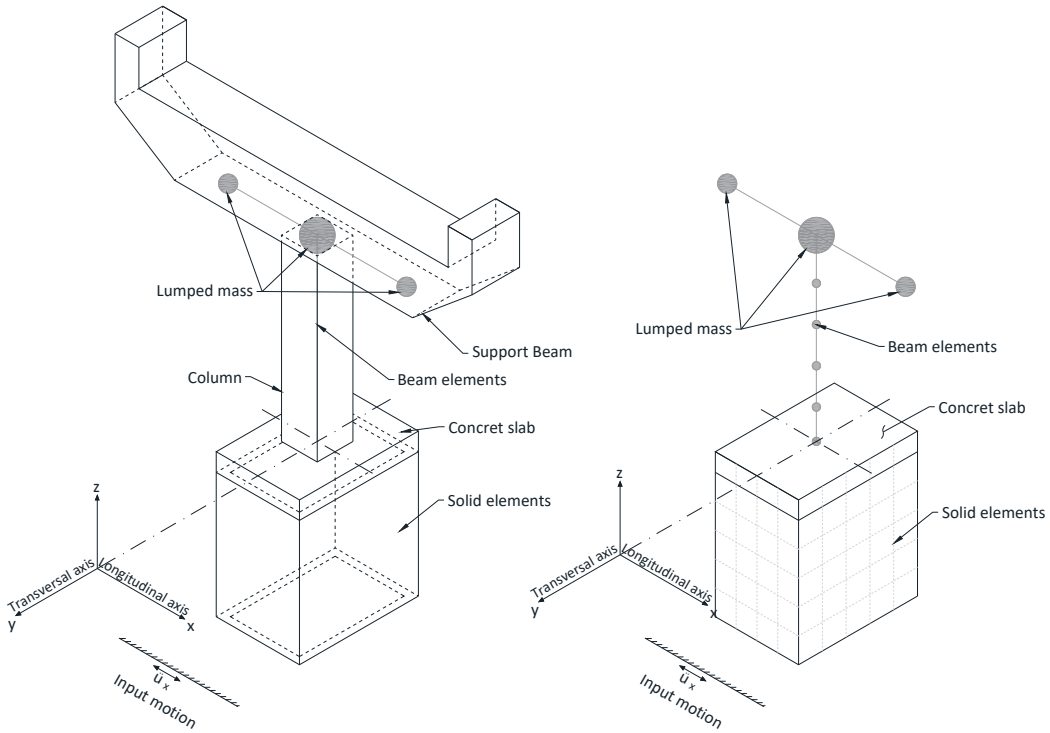

Figure 14. Structural elements used in the numerical model for the structured cell.

 doi:10.20944/preprints202605.0415.v1

5. Results

Figure 15 compares the pore pressure and effective stress histories obtained at 7.0 m depth for each foundation alternative (i.e., within the potentially liquefiable sand). A clear reduction in pore pressure generation is observed when the structured cell is used, with reductions of 42% and 25% compared to the footing and pile alternatives, respectively, during the most intense phase of shaking. This reduction is accompanied by a smaller decrease in effective stress, indicating that the soil retains a greater portion of its strength during shaking compared to the footing and pile cases.

The spatial distribution of pore pressure reinforces this picture. Figures 16 to 19 present contour plots at two key instants: the moment of maximum ground acceleration and the end of shaking. In the footing and pile cases, high pore pressure zones tend to concentrate within the liquefiable layer and spread across a considerable portion of the foundation footprint. The structured cell, on the other hand, produces a more contained pattern. The perimeter walls appear to limit the extent of the elevated-pressure zone, keeping the most critical conditions confined to a smaller volume of soil. By the end of the earthquake, the contrast is still visible: the structured cell ends shaking with a markedly different pressure field than the other two systems, with reductions of roughly 35% and 30% relative to the footing and pile foundations, respectively.

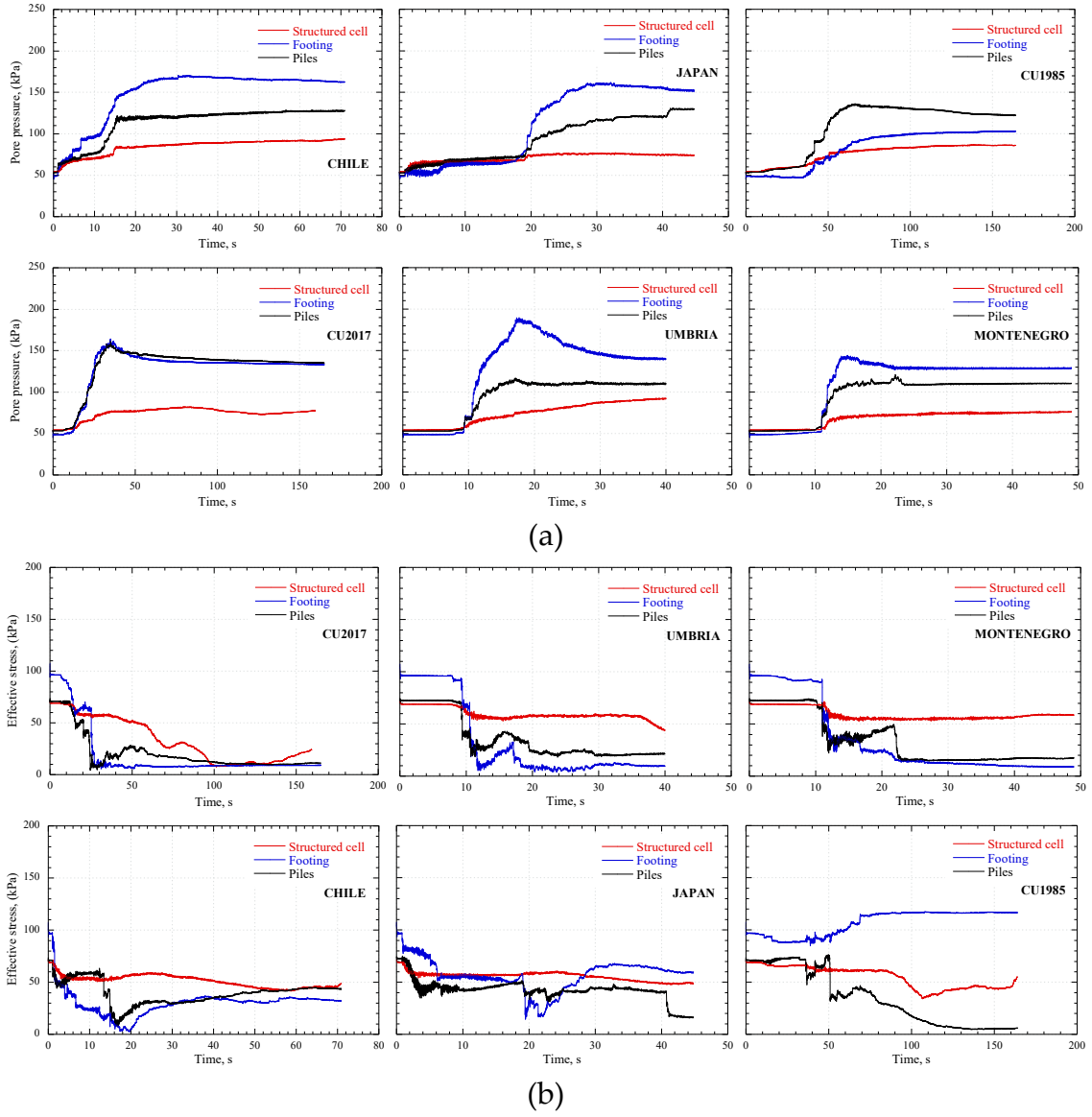

Figure 15. (a) Pore pressure and (b) effective stress histories obtained at a depth of 7.0 m for all cases.

 doi:10.20944/preprints202605.0415.v1

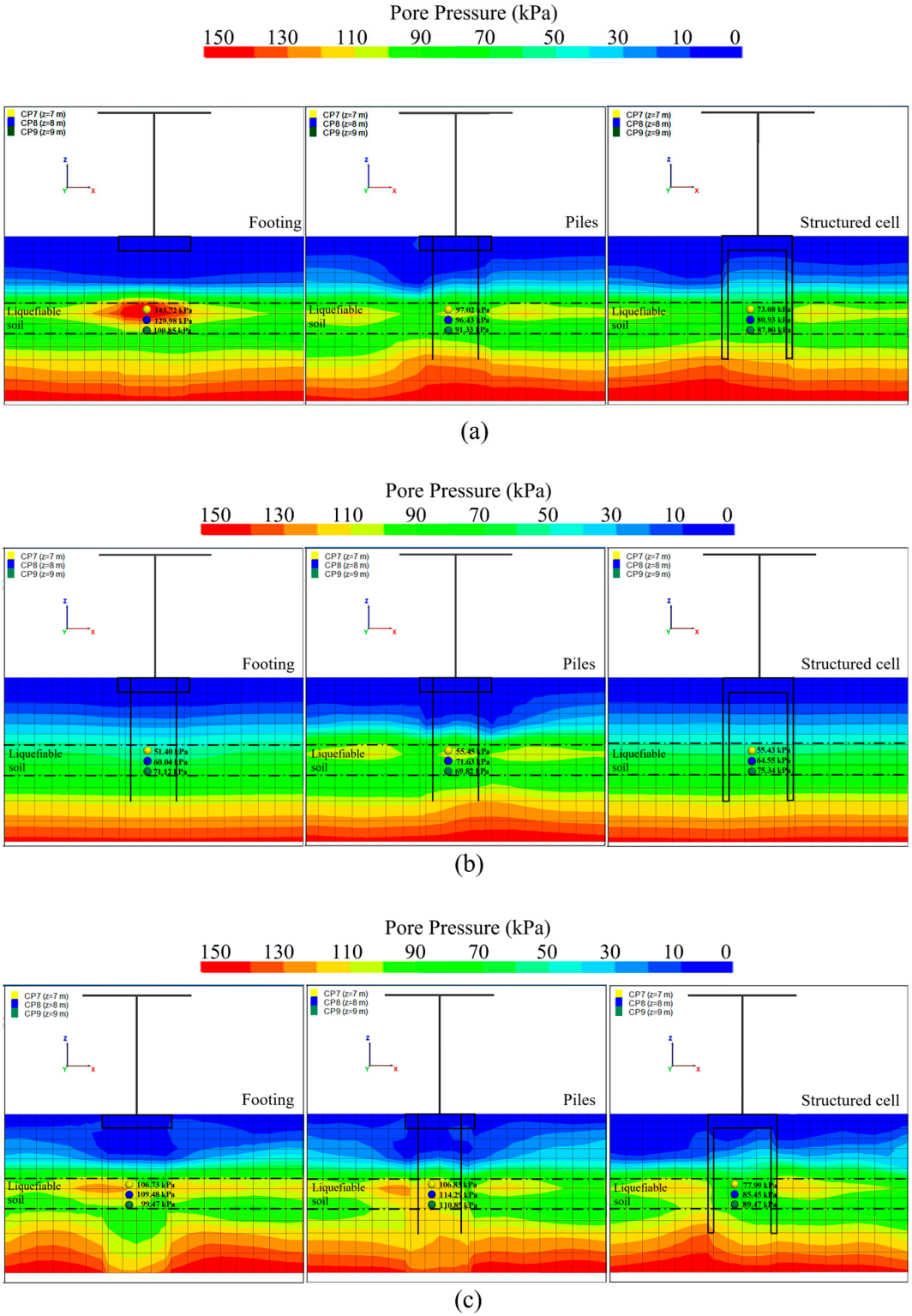

Figure 16. Pore pressure contour at the instant of maximum acceleration of the ground motion for (a) Umbria, (b) Montenegro, and (c) CU17.

 doi:10.20944/preprints202605.0415.v1

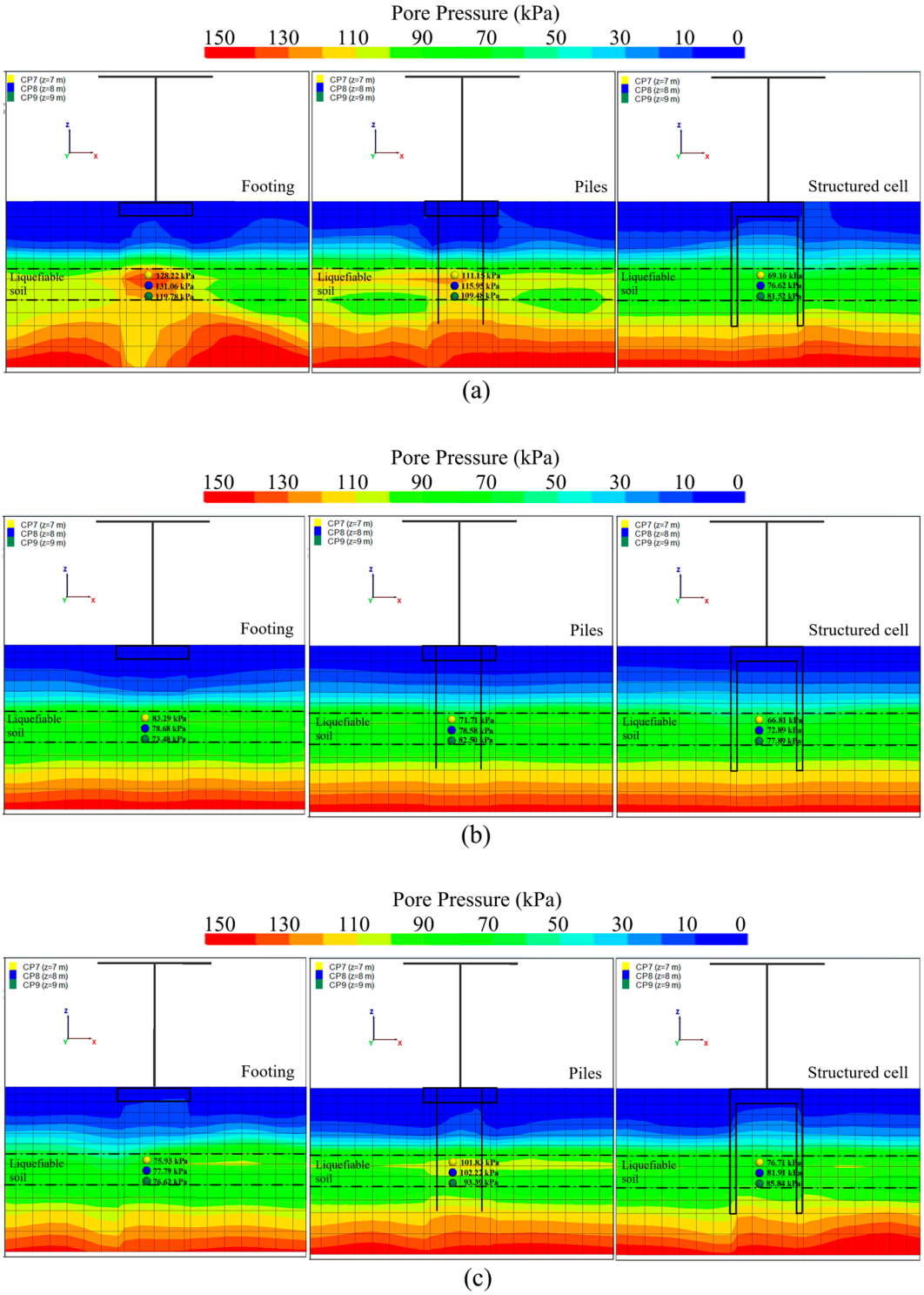

Figure 17. Pore pressure contour at the instant of maximum acceleration of the ground motion for (a) Japan, (b) Chile, and (c) CU85.

 doi:10.20944/preprints202605.0415.v1

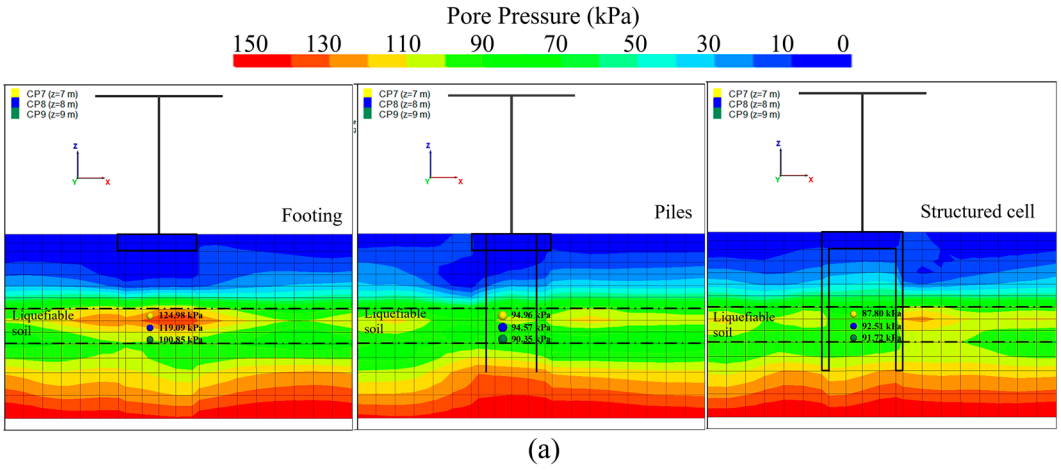

(a)

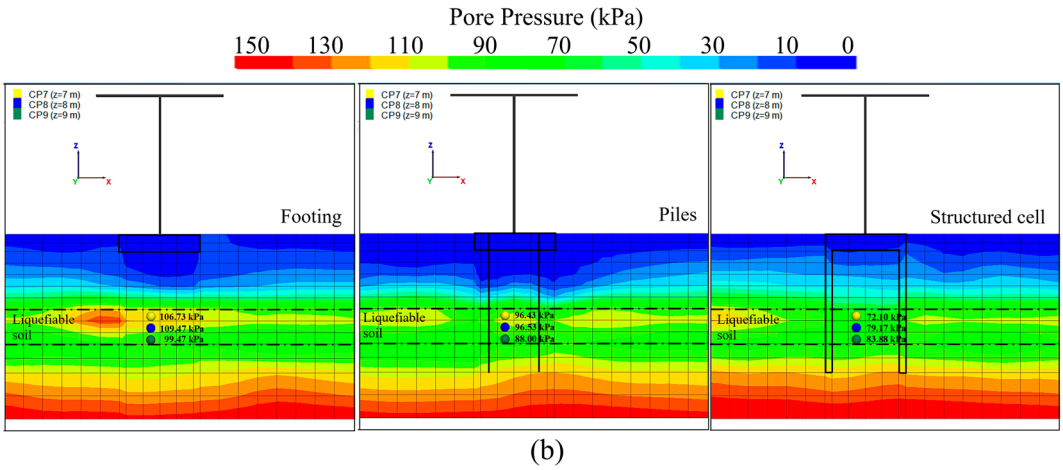

(b)

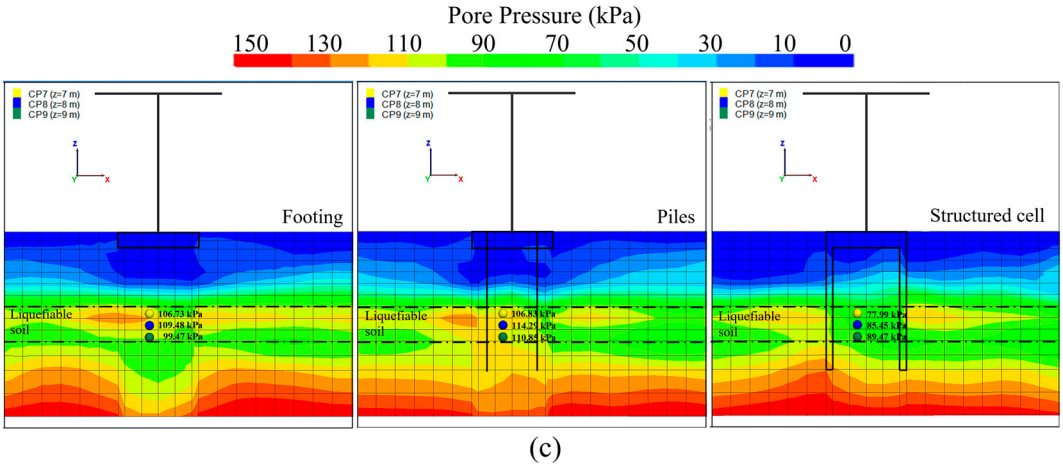

(c)

Figure 18. Pore pressure contour at the end of the ground motion for (a) Umbria, (b) Montenegro, and (c) CU17.

 doi:10.20944/preprints202605.0415.v1

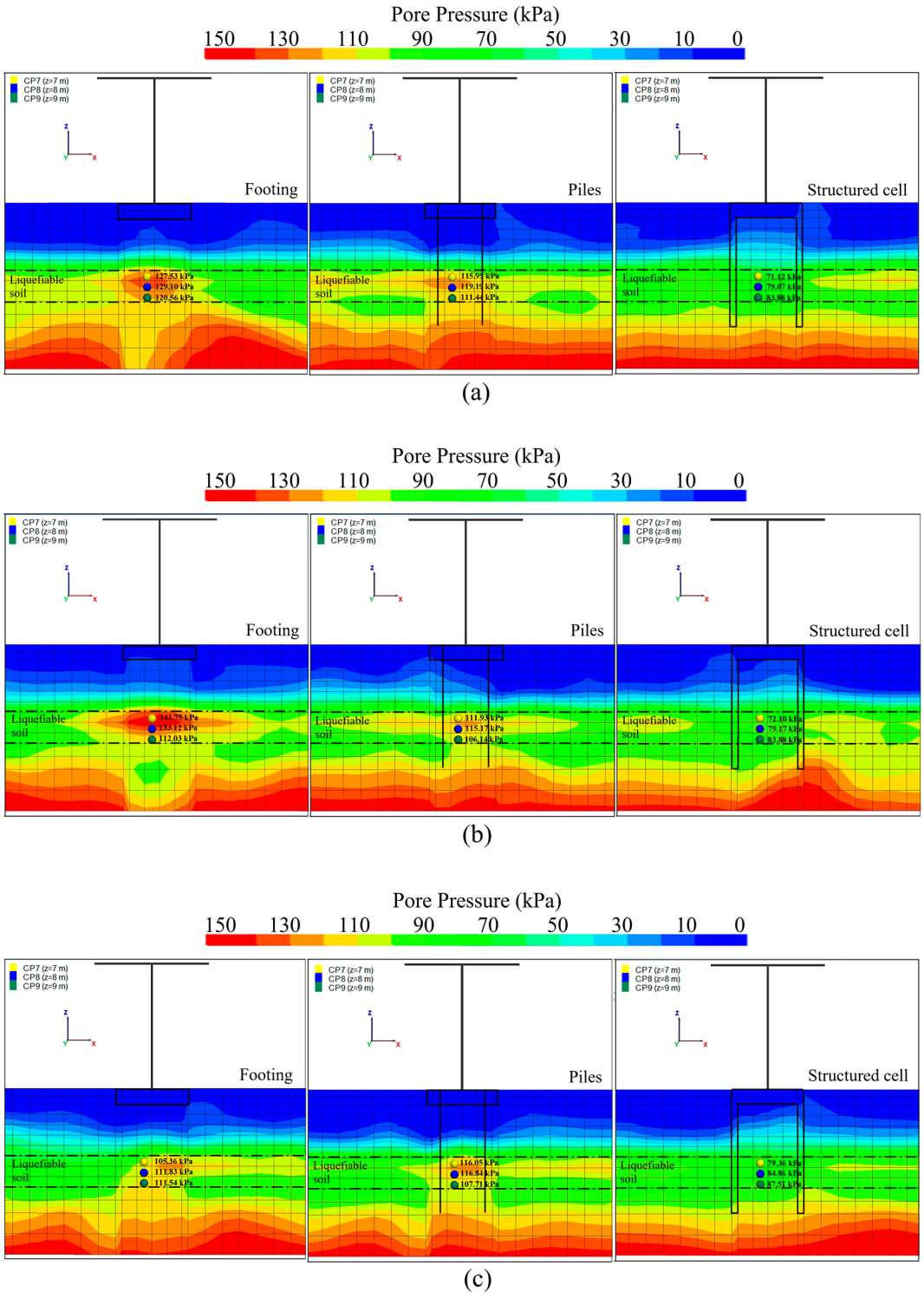

Figure 19. Pore pressure contour at the end of the ground motion for (a) Japan, (b) Chile, and (c) CU85.

Figures 20 and 21 present the excess pore pressure ratio, r_u, where $r_u = \Delta u/\sigma'$. Δu is the excess pore pressure, and σ' is the effective initial confinement stress obtained at different depths of the soil profile (i.e., 7, 8, and 9 m). When r_u> 0.90, significant liquefaction effects are expected. It is observed that, for a depth of 7 m (i.e., within the potentially liquefiable sand), the excess pore pressure ratio reaches total liquefaction (r_u =1.0) at different times for both footing and pile foundations. In contrast, the structured cell maintains r_u values below critical thresholds (r_u <0.90 in most cases), suggesting that the onset of liquefaction is delayed or mitigated. This response is consistent with a reduction in cyclic shear strain accumulation within the confined soil, which is the primary driver of contractive volumetric strains and subsequent pore pressure generation.

 doi:10.20944/preprints202605.0415.v1

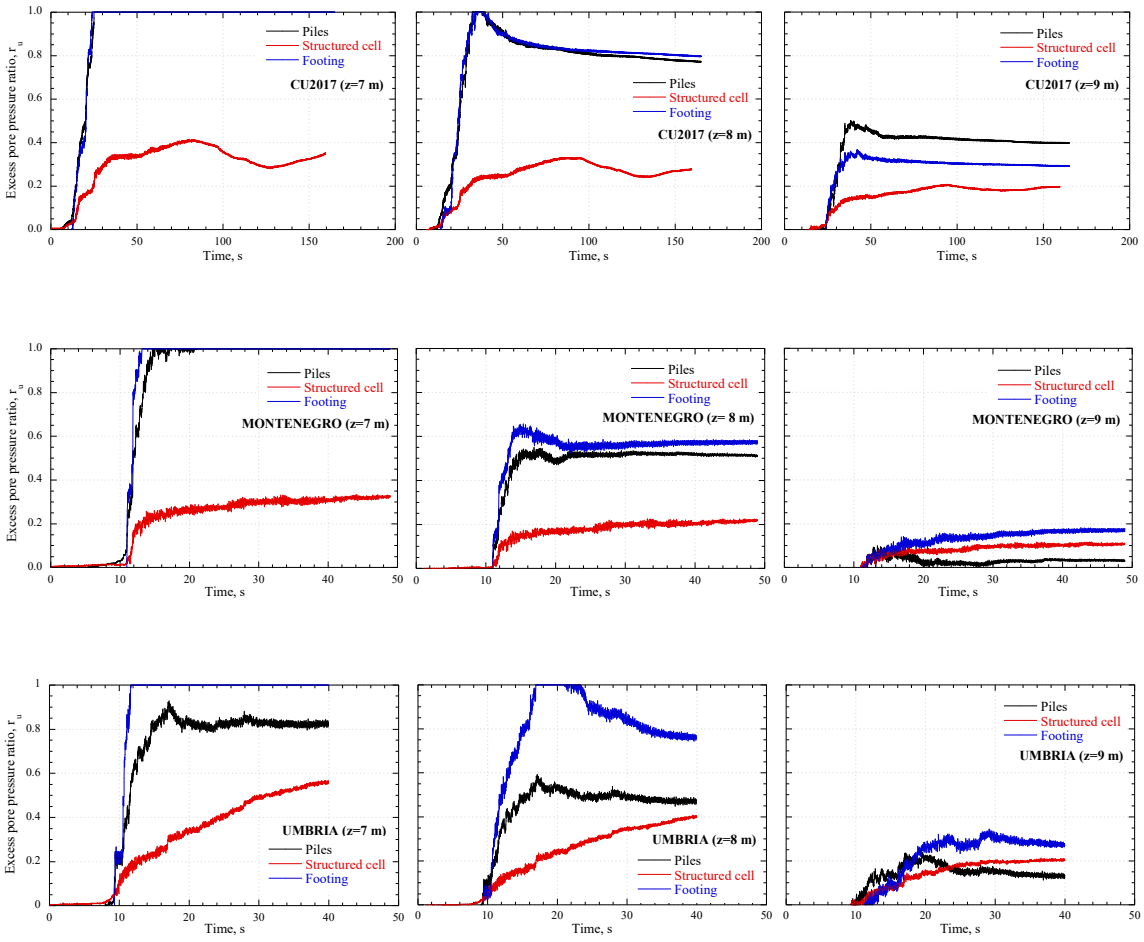

Figure 20. Excess pore pressure ratio obtained at the center of the liquefiable stratum at 7.0 m, 8.0 m, and 9.0 m depths, for intraplate earthquakes.

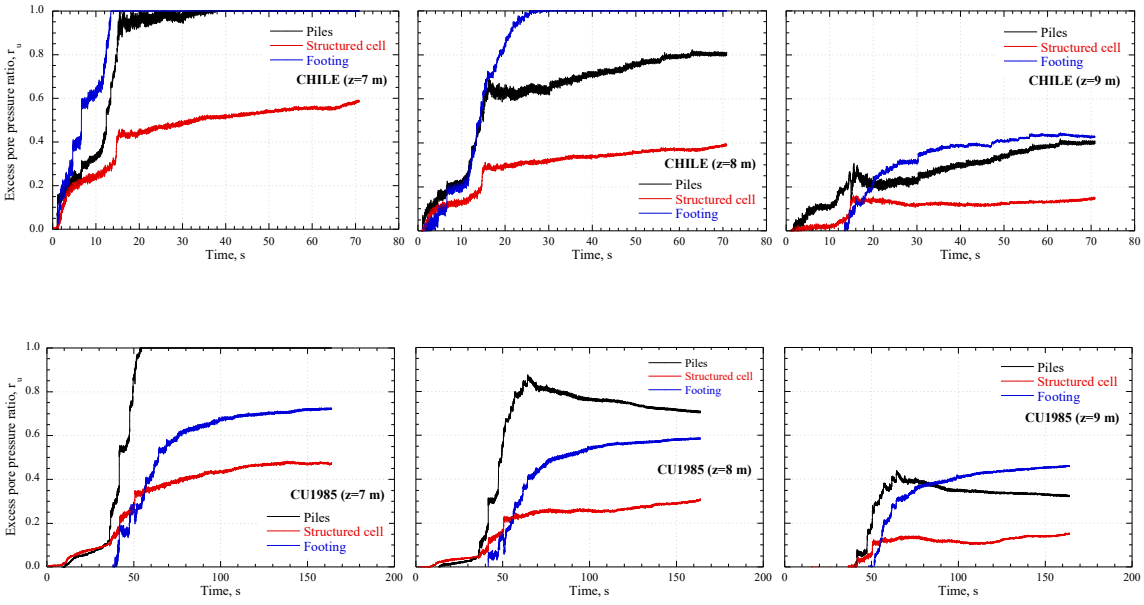

Preprints.org (www.preprints.org) | NOT PEER-REVIEWED | Posted: 7 May 2026 doi:10.20944/preprints202605.0415.v1

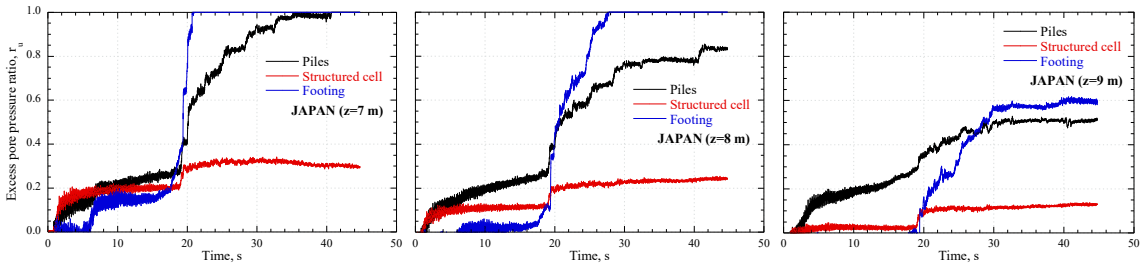

Figure 21. Excess pore pressure ratio obtained at the center of the liquefiable stratum at 7.0 m, 8.0 m, and 9.0 m depths, for interplate earthquakes.

Figures 22 and 23 show the distribution of shear strain increments for the different foundation systems. For the footing and pile foundations, pronounced strain localization develops within the liquefiable layer, particularly near the soil–foundation interface, coinciding with the depths where r_u reaches unity and effective stress approaches zero. When the structured cell is used, these strain concentrations are significantly reduced, and deformation appears more uniformly distributed across the confined soil volume rather than concentrated in narrow zones. This direct correspondence between reduced shear strain and lower pore pressure supports the interpretation that the structured cell primarily kinematically restrains cyclic shear deformation within the enclosed soil, rather than enhancing drainage or altering the soil's intrinsic properties.

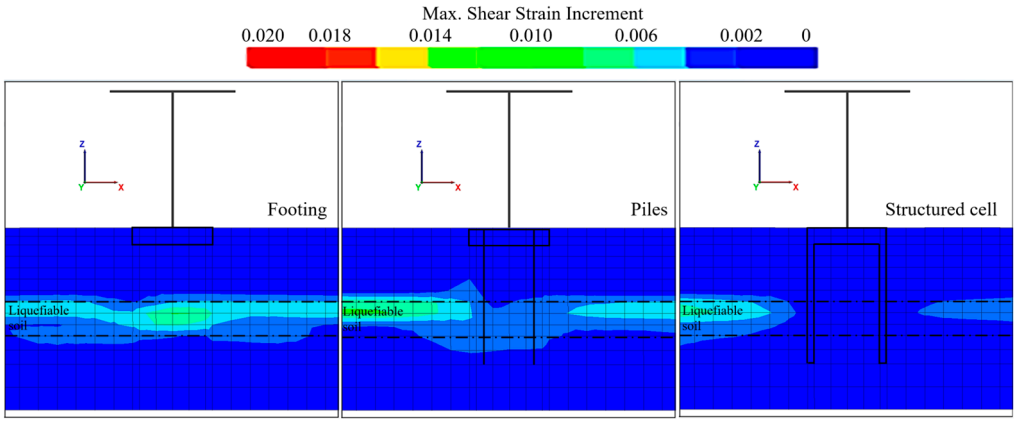

(a)

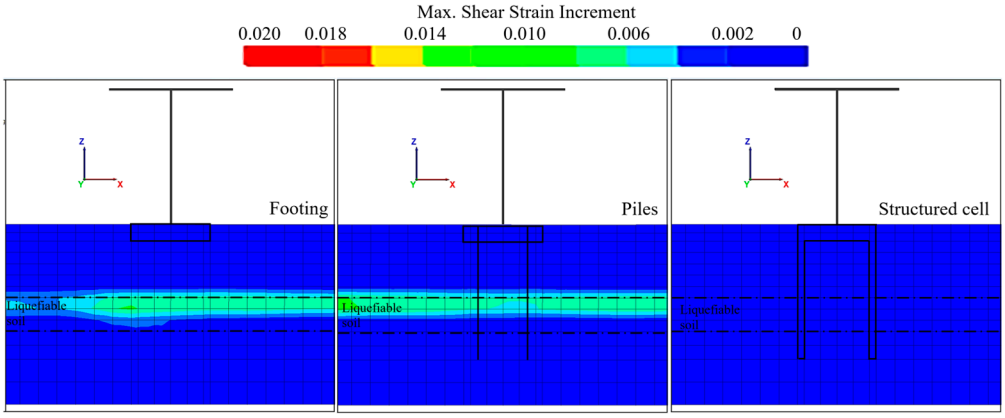

(b)

 doi:10.20944/preprints202605.0415.v1

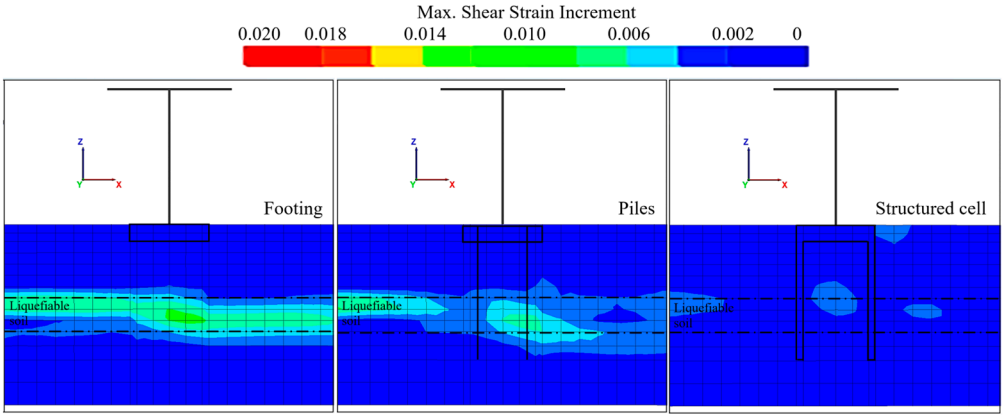

(c)

Figure 22. Shear strain increment for (a) Umbria, (b) Montenegro, and (c) CU17 earthquakes.

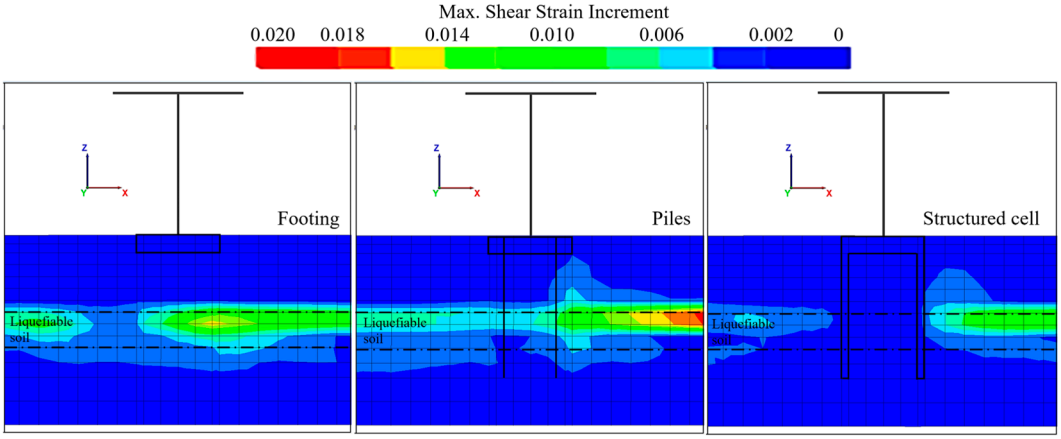

(a)

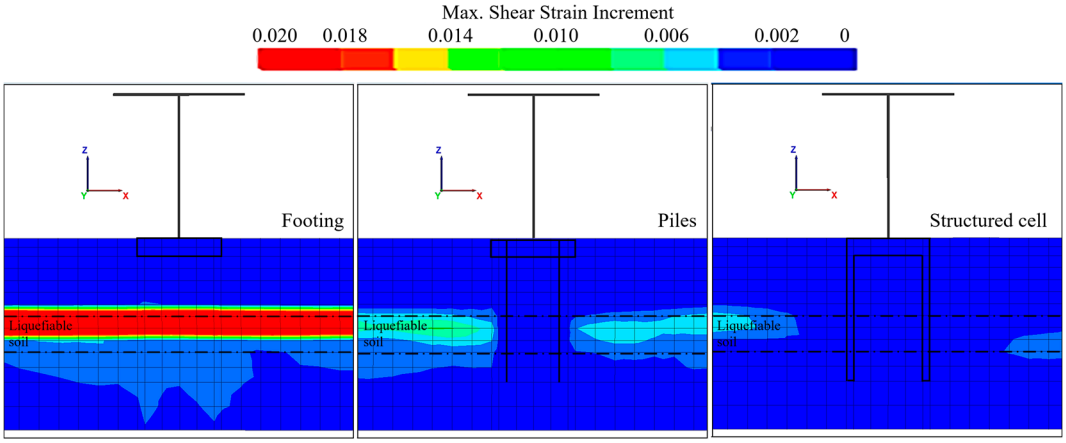

(b)

 doi:10.20944/preprints202605.0415.v1

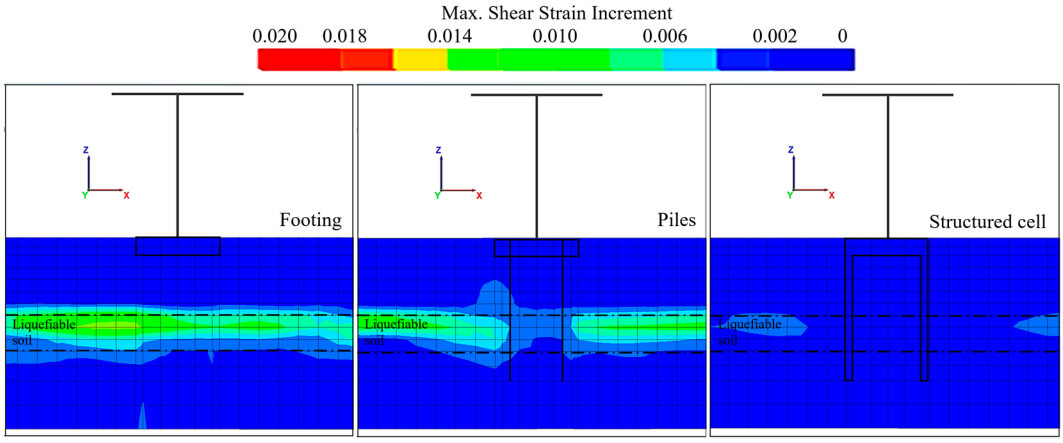

(c)

Figure 23. Shear strain increment for (a) Chile, (b) Japan, and (c) CU85 earthquakes.

Figure 24 presents the maximum acceleration recorded at the bridge deck. The structured cell reduces peak acceleration by up to 25% compared to conventional foundations. This reduction can be associated with a more stable soil response: as the structured cell prevents the complete loss of soil stiffness within the liquefiable layer, the soil profile retains a higher shear wave velocity, reducing amplification effects that typically arise when a low-impedance liquefied layer underlies a stiffer surface crust. In contrast, the conventional foundations experience a sharp stiffness contrast between the liquefied soil and the overlying structure, which can trap seismic energy and amplify certain frequency components.

Likewise, the energy that reaches the bridge deck, expressed as the Housner intensity of its motion, S_I (ξ), is presented in Figure 25. Housner Intensity is an energy-based intensity measure, calculated for each earthquake record as the integral of the pseudo-velocity spectrum (5% damping) for periods between 0.1 and 2.5 s, defined by Eq. (6).

$$S_I(\xi) = \int_{0.1}^{2.5} PSV\ (\xi, T)\, dT \tag{6}$$

where ξ, is the damping ratio of a structure, PSV is the pseudo-velocity spectrum, and T is the period range of 0.1 to 2.5s. The Housner spectral intensity was computed at the upper-deck bridge for each foundation studied as a measure of the system's energy. The results indicate a slight reduction in the energy transmitted to the structure when using the structured cell. Although the decrease is modest (on the order of 3%), it is worth noting that Housner intensity integrates spectral response over a broad period range (0.1–2.5 s). The fact that the reduction is measurable, albeit small, suggests that the benefit of the structured cell is primarily concentrated in the shorter-period components of the response, where the preservation of soil stiffness has the greatest influence. This modest reduction in energy demand is consistent with the more significant reduction observed in peak acceleration.

Overall, the results suggest that the improved performance of the structured cell is not only due to increased stiffness but also to its ability to control the deformation mechanisms that govern liquefaction. In particular, by limiting shear strain accumulation, disrupting pore water migration, and modifying deformation patterns, the system reduces pore pressure generation and preserves effective stress within the soil. These multiple, coupled effects explain why the structured cell outperforms both the footing and the pile group across all the seismic scenarios examined.

 doi:10.20944/preprints202605.0415.v1

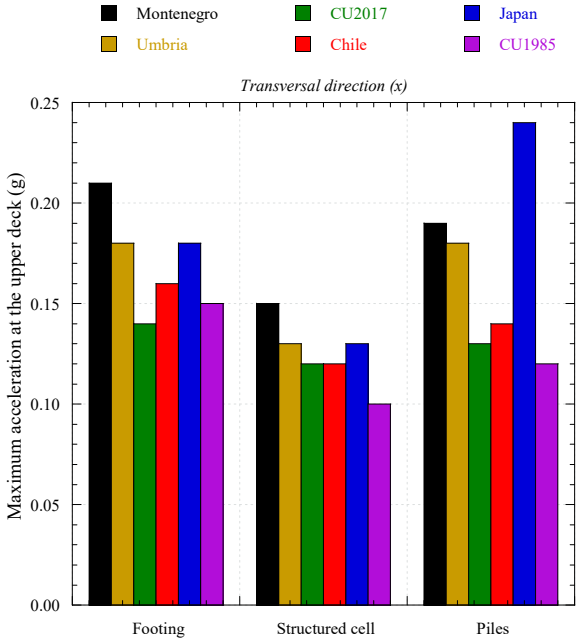

Figure 24. Maximum acceleration obtained at the upper deck bridge for the transversal (X) direction.

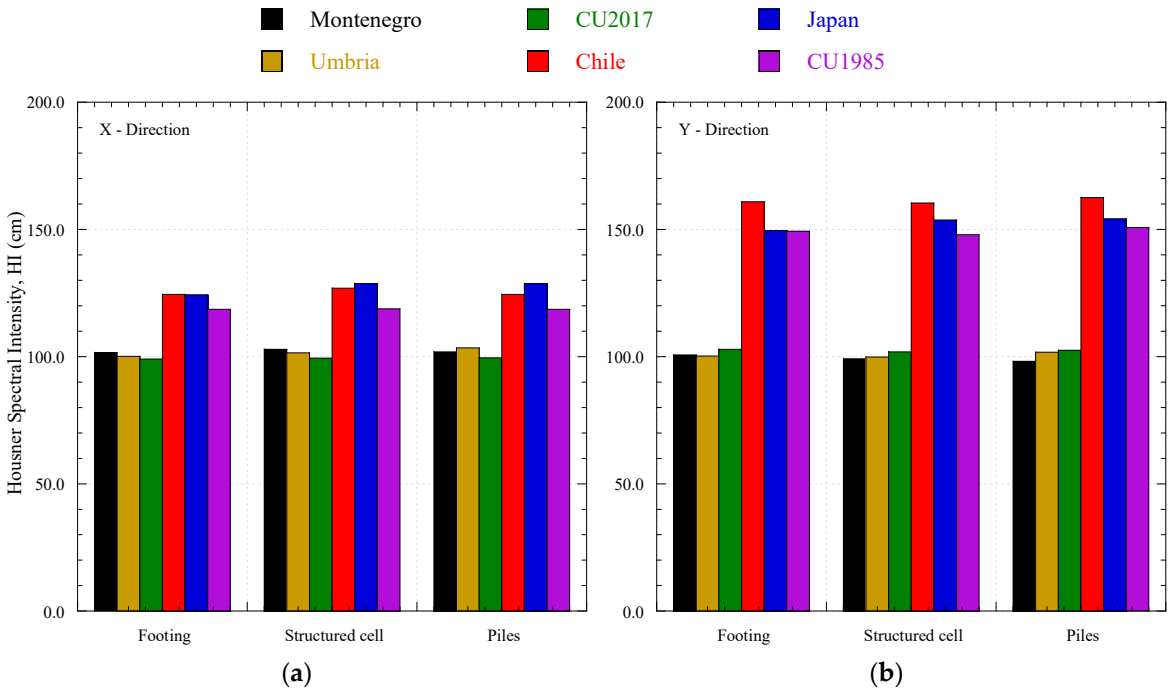

Figure 25. Housner Intensity at the structure for a) transversal (X) and b) longitudinal (Y) directions.

From a design perspective, these findings highlight the importance of considering deformation control alongside strength-based approaches when addressing liquefaction problems. Structured confinement systems may therefore offer a practical alternative for improving foundation performance in seismic regions.

6. Conclusions

This study evaluated the seismic performance of three foundation alternatives, a conventional spread footing, a pile group, and a structured cell, for a bridge founded on a potentially liquefiable

 doi:10.20944/preprints202605.0415.v1

soil profile. Three-dimensional finite-difference analyses were conducted under the action of both intraplate and interplate earthquakes. The key findings are summarized as follows:

A primary finding of this work is that the structured cell foundation mitigates liquefaction primarily through a confinement mechanism rather than through drainage effects. The rigid perimeter walls and top slab kinematically restrain the enclosed soil mass, directly limiting the development of large cyclic shear strains that drive contractive volumetric strains and excess pore pressure generation. This represents a fundamentally different mitigation paradigm from traditional drainage-based or soil-improvement techniques.

This confining effect quantitatively translates into a highly effective suppression of liquefaction indicators. Compared to conventional systems, the structured cell reduced peak excess pore pressure by up to 42% relative to the spread footing and 25% relative to the pile group. These results are consistent with the quantified reductions in shear strain accumulation and effective stress loss within the liquefiable layer. Under the analyzed seismic conditions, the system significantly delayed or prevented the onset of full liquefaction, maintaining excess pore pressure ratios below the critical threshold of 0.90, whereas conventional foundations reached values approaching $r_u \approx 1.0$.

Preserving soil strength and stiffness at the foundation level directly benefits the superstructure's seismic response. The composite soil–cell system reduced peak accelerations transmitted to the bridge deck by up to 25% and led to a slight decrease in seismic energy demand, as measured by Housner intensity. Significant reductions in lateral displacements and settlements were also observed, indicating improved global system stability and post-earthquake serviceability.

Superior performance is attributed to the structural cell's ability to modify the fundamental mechanisms governing liquefaction. By restricting cyclic shear strain accumulation, the structured cell reduces deformation localization and preserves effective stresses within the confined soil mass, effectively interrupting the sequence of processes that lead to strength loss.

These findings highlight the importance of integrating deformation-control mechanisms alongside traditional strength-based approaches in the design of foundations for liquefiable soils. From an engineering standpoint, the structured cell may represent a technically sound alternative for bridge support systems in seismic zones, particularly where limiting post-earthquake deformations and ensuring functionality are critical performance objectives.

However, these results should be interpreted within the scope of this study, acknowledging the use of empirically derived dynamic soil properties, the simplified nature of the constitutive model, and the absence of experimental validation. Future work should focus on parametric optimization of structural cell geometry, experimental validation, and the development of practical design methodologies that incorporate the identified confinement mechanism.

Author Contributions: Conceptualization, J.M.M.; methodology, J.M.M. and N.O.; software, N.O.; validation, J.M.M. and N.O.; formal analysis, N.O.; investigation, J.M.M. and N.O.; resources, J.M.M.; data curation, N.O.; writing—original draft preparation, N.O.; writing—review and editing, J.M.M. and N.O.; visualization, N.O. All authors have read and agreed to the published version of the manuscript.

Funding: This research received no external funding.

Institutional Review Board Statement: Not applicable.

Informed Consent Statement: Not applicable.

Data Availability Statement: The original contributions presented in this study are included in the article. Further inquiries can be directed to the corresponding author.

Conflicts of Interest: The authors declare no conflicts of interest.

 doi:10.20944/preprints202605.0415.v1

References

1. Hamada, M. (1992). Large ground deformations and their effects on lifeline: 1964 Niigata Earthquake. Proceedings, Case Studies of Liquefaciton and Lifeline Performance During Past Earthquakes, Japanese Case Studies, 1.
2. Yang, Z., & Zhang, X. (2012). Seismic performance and design of bridge foundations in liquefiable ground with a frozen crust.
3. Mitchell, J. K., and F. J. Wentz. 1991. Performance of improved ground during the Loma Prieta earthquake. Berkeley, CA: Earthquake Engineering Research Center, Univ. of California at Berkeley.
4. Akai, K., Bray, J. D., Boulanger, R. W., & Christian, J. T. (1997). Geotechnical Reconnaissance of the Effects of the January 17, 1995, Hyogoken-Nanbu Earthquake, Japan. Diane Publishing.
5. Turner, B. J., Brandenberg, S. J., & Stewart, J. P. (2015). Influence of kinematic SSI on foundation input motions for pile-supported bridges. Pacific Earthquake Engineering Research Center.
6. Ledezma, C. A., & Bray, J. D. (2008). Performance-based earthquake engineering design evaluation procedure for bridge foundations undergoing liquefaction-induced lateral ground displacement. Pacific Earthquake Engineering Research Center.
7. Valsamis, A. I., Bouckovalas, G. D., & Chaloulos, Y. K. (2012). Parametric analysis of single pile response in laterally spreading ground. Soil Dynamics and Earthquake Engineering, 34(1), 99-110.
8. Elgamal, A., Yan, L., Yang, Z., y Conte, J. P. (2008). Three-dimensional seismic response of Humboldt Bay bridge-foundation-ground system. J of Struct Eng, 134(7), 1165-1176.
9. Ashford, S. A., Boulanger, R. W., & Brandenberg, S. J. (2011). Recommended design practice for pile foundations in laterally spreading ground. Pacific Earthquake Engineering Research Center.
10. Tasiopoulou, P., Gerolymos, N., Tazoh, T., & Gazetas, G. (2013). Pile-group response to large soil displacements and liquefaction: centrifuge experiments versus a physically simplified analysis. Journal of geotechnical and geoenvironmental engineering, 139(2), 223-233.
11. Mohanty, P., Xu, D., Biswal, S., & Bhattacharya, S. (2021). A shake table investigation of dynamic behavior of pile supported bridges in liquefiable soil deposits. Earthquake Engineering and Engineering Vibration, 20(1), 1-24.
12. Karamitros, D. K., Bouckovalas, G. D., Chaloulos, Y. K., & Andrianopoulos, K. I. (2013). Numerical analysis of liquefaction-induced bearing capacity degradation of shallow foundations on a two-layered soil profile. Soil Dynamics and Earthquake En-gineering, 44, 90-101.
13. Boulanger, R. W., Idriss, I. M., (2014). "CPT and SPT based liquefaction triggering procedures". Report No. UCD/CGM-14/01. Center for Geotechnical Modeling. Department of Civil & Environmental Engineering. College of Engineering. University of California at Davis, april 2014.
14. Hausmann, M. 1990. Engineering principles of ground modification: International addition. New York: McGraw-Hill.
15. Huang, Y., and Z. Wen. 2015. "Recent developments of soil improvement methods for seismic liquefaction mitigation." Nat. Hazards 76 (3): 1927–1938. https://doi.org/10.1007/s11069-014-1558-9.
16. Seed, R. B., K. O. Cetin, R. E. S. Moss, A. M. Kammerer, J. Wu, J. M. Pestana, and M. F. Riemer. 2001. "Recent advances in soil liquefaction engineering and seismic site response evaluation." In Proc., 4th Int. Conf. on Recent Advances in Geotechnical Earthquake Engineering and Soil Dynamics and Symp. in Honor of Professor W. D. Liam Finn, 1–45. Rolla, Missouri: Missouri University of Science and Technology.
17. Indraratna, B., Chu, J., & Rujikiatkamjorn, C. (2015). Ground improvement case histories: compaction, grouting and geosynthetics. Butterworth-Heinemann, pp 3-50.
18. Zhou, Y. G., Liu, K., Sun, Z. B., & Chen, Y. M. (2021). Liquefaction mitigation mechanisms of stone column-improved ground by dynamic centrifuge model tests. Soil Dynamics and Earthquake Engineering, 150, 106946.
19. Tominsawa, K., & Miura, S. (2013). A design verification method for pile foundations used in combination with solidified improved columns. In Proceedings of the 18th International Conference on Soil Mechanics and Geotechnical Engineering, Paper (No. 2021).

 doi:10.20944/preprints202605.0415.v1

20. Sharma, M., Satyam, N., y Reddy, K. R. (2020). "State of the Art Review of Emerging and Biogeotechnical Methods for Liquefaction Mitigation in Sands". Journal of Haz-ardous, Toxic, and Radioactive Waste, 25(1), 03120002.
21. Itasca Consulting Group (2009) "FLAC3D Fast Lagrangian Analysis of Continua in 3 dimensions, Ver. 5.0 User's Manual, Minneapolis, Minnesota, USA: s.n.
22. Imai, T., 1977. P and S wave velocities of the ground in Japan. Proceedings of IX International Conference on Soil Mechanics and Foundation Engineering, 2, pp. 127-132.
23. Pitilakis, K. et al., 1999. Geotechnical and geophysical description of Euro-Seistests, using field and laboratory test, and moderate strong ground motions. J Earth Eng 3, pp. 381-409.
24. Dickmen, U., 2009. Statistical correlations of shear wave velocity and penetration resistant for soils. Journal of Geophysics and engineering 6, p. 4167.
25. Zhang, J., Andrus, R. D., & Juang, C. H. (2005). Normalized shear modulus and material damping ratio relationships. Journal of geotechnical and geoenvironmental engineering, 131(4), 453-464.
26. Kumar, S. S., Krishna, A. M., & Dey, A. (2017). Evaluation of dynamic properties of sandy soil at high cyclic strains. Soil Dynamics and Earthquake Engineering, 99, 157-16.
27. Vucetic, M. y Dobry, R., (1991). "Effect of soil plasticity on cyclic response". Journal of Geotech. Engineering., ASCE, Vol. 114(1) pp. 89-107.
28. Kallioglou, P., Tika, T. H., & Pitilakis, K. (2008). Shear modulus and damping ratio of cohesive soils. Journal of Earthquake Engineering, 12(6), 879-913.
29. Guerreiro, P., Kontoe, S., & Taborda, D. (2012, September). Comparative study of stiffness reduction and damping curves. In 15th World Conference on Earthquake En-gineering (pp. 1-10).
30. Singh, S.K., Ordaz, M., Pérez-Campos, X., Iglesias, A., 2015. Intraslab versus Inter-plate Earthquakes as Recorded in Mexico City: Implications for Seismic Hazard. Earthquake Spectra. 31 (2), 795–812.
31. Zúñiga, F.R., Suárez, G., 2017. A first-order seismotectonic regionalization of Mex-ico for seismic hazard and risk estimation. J Seismol 2017 (21), 1295–1322. https://doi. org/10.1007/s10950-017-9666-0.
32. NTCS. 2020. Normas Técnicas Complementarias para Diseño por Sismo. Gaceta Oficial de la Ciudad de México.
33. Singh, S.K., Mena, E., Castro, R., Carmona, C., 1988. Prediction of peak, horizontal ground motion parameters in Mexico City from coastal earthquakes. Geofis. Int. 27, 111–129.
34. Ordaz, M. 2016. Normas de Diseño por Sismo en México DF: algunas novedades interesantes. Alternativas. ISSN: 1390-1915 • VOL. 17 • N.O 3 • 2016. • 106-115.
35. ASCE, 2010. Minimum Design Loads for Buildings and Other Structures. ASCE/SEI Standard 7–10. American Society of Civil Engineers.
36. Lilhanand Ky & Tseng WS. 1988. Development and application of realistic earth-quake timehistories compatible with multiple damping response spectra. In Proceed-ings of the9th world conference on earthquake engineering, Tokyo, Japan 1988(2): 819–824.7
37. Abrahamson NA. 2000. State of the practice of seismic hazard evaluation. Pro-ceedings of GeoEng 2000, Melbourne, 19–24 November 2000(1): 659–685.
38. Seed HB, Idriss IM, (1970). Soil moduli and damping factors for dynamic response analysis. (UBC/EERC-70/10). Berkeley: University of California.
39. Seed, H.B., Wong, R.T., Idriss, M, y Tokimatsu, K., (1986). Moduli and damping factors for dynamic analyses of cohesionless soils. Geot Eng Div, Vol. 112(11): pp 1016-1032.
40. Youd, T. L., e Idriss, I. M., eds. (2001). Liquefaction resistance of soils. Journal of Geotechnical and Geoenvironmental Engineering, Vol. 127, No. 4, April 2001
41. Idriss, I. M., and Boulanger, R.W. (2008). "Soil liquefaction during earthquakes". Monograph MNO-12, Earthquake Engineering Research Institute, Oakland, CA.
42. Boulanger, R. W., Idriss, I. M., (2014). "CPT and SPT based liquefaction triggering procedures". Report No. UCD/CGM-14/01. Center for Geotechnical Modeling. Department of Civil & Environmental Engineering. College of Engineering. University of California at Davis, april 2014.
43. Schnabel, P. B., Lysmer, J., and Seed, H. B. (1972). ''A computer program for earthquake response analysis of horizontally layered sites.'' Rep. No. EERC 72-12, UC Berkeley.

 doi:10.20944/preprints202605.0415.v1

44. Kuhlemeyer RL, Lysmer J. 1973. Finite element method Accuracy for wave propagation problems. Soil Dynamics and Earthquake Engineering 1973(99): 421–427.
45. Finn, W., Martin, G. & Lee, K., 1975. An Effective Stress Model for Liquefaction. Journal of the Geotechnical Engineering Division, 103(6), pp. 517-533.
46. Byrne, P. M., 1991. A Cyclic Shear-Volume Coupling and Pore-Pressure Model for Sand. Proc 2 Int Conf on Recent Advances in Geot Earth Eng and Soil Eng, Issue 1, pp. 47-55.
47. Garcia Diez, J. L., Gonzalez Galindo, J., Soriano Peña, A., & Universidad Politécnica de Madrid. (2019). Adjustment of a numerical model for pore pressure generation during an earthquake. Plos one, 14(9), e0222834.
48. Iraji, A., & Osouli, A. (2020). Liquefaction Numerical Analysis of a Cantilevered Retaining Wall Using a Simple Finn-Byrne Model. In Geo-Congress 2020: Geotechnical Earthquake Engineering and Special Topics (pp. 41-50). Reston, VA: American Society of Civil Engineers.
49. Chou, J. C., Yang, H. T., & Lin, D. G. (2021). Calibration of Finn Model and UBCSAND Model for Simplified Liquefaction Analysis Procedures. Applied Sciences, 11(11), 5283.
50. Martínez-Galván, S. A., & Romo-Organista, M. P. (2013). Capacidad de carga tri-dimensional de celdas estructuradas apoyadas en suelo cohesivo: método de análisis simplificado. Ingeniería, investigación y tecnología, 14(3), 399-412.
51. Mayoral, J. M., and Romo, M. P. (2015). Seismic response of bridges with massive foundations. Soil Dynamics and Earthquake Engineering, 71, 88-99.